Design and evaluation of navigation and control algorithms for spacecraft formation flying missions

Laura Perea Virgili

Design and evaluation of navigation and control algorithms for spacecraft formation flying missions

Laura Perea Virgili

Facultat de Matemàtiques

Universitat de Barcelona

Programa de doctorat de matemàtiques. Bienni 2005-2006.

Memoria presentada per obtenir el grau de
Doctor en Matemàtiques per la Universitat de Barcelona.

Director de tesis: Pedro Elosegui Larrañeta, CSIC
Tutor: Gerard Gómez Muntané, UB

A la meva família, passat, present i futur.

Contents

Agraïments / Acknowledgments

Voldria agrair a tota la meva família el suport constant i la plena confiança que han dipositat sempre en mi. És gracies a ells i als valors que m'han transmès que he pogut arribar fins aquí.

No puc oblidar als companys i amics que m'han ajudat en l'elaboració d'aquesta tesis. A la Gemma Colomé, qui m'ha animat i servit d'exemple, a la Júlia de Juan, amb qui he compartit l'experiència del doctorat i a tots els companys de l'IEEC.

Voldria mostrar també la meva gratitud vers Gerard Gómez. A més a més de la tutela, li voldria agrair especialment els seus consells, que sempre he considerat sincers, i d'un valor inestimable.

I want to thank Pedro Elosegui for his clever counseling, remarkable positiveness, and easygoing disposition. I specially appreciate his constant encouragement for research mobility, and the large degree of autonomy that he allowed me to conduct this research.

Special thanks to the coauthors Prof. Jonathan How, Louis Breger, Simone D'Amico, and Jean-Sébastian Ardaens for their close collaboration, and constant support.

Fortunately, the PhD process does not limit to the research but it also allowed me to make new friends and grow both professionally and personally. I will never forget the good memories with Pedro Elosegui and his cute family, Jonathan de Wolff, Christina Donivan, and Srinivas Turaga in Cambridge, MA; with Simone D'Amico, Jean-Sébastien Ardaens, Cécile Renaudie, Miquel Garcia, Oliver Montenbruck and his family, and Marc Höpfner in Munchen; and many others around who made me feel comfortable and enjoy their cities during my visits abroad.

Riudoms,

13 de juny de 2010

Declaration

I hereby certify that this research has been performed by Laura Perea Virgili and supervised by myself.

Barcelona, June 13, 2010

Dr. Pedro Elosegui Larrañeta
Instituto de Ciencias del Espacio – Consejo Superior de Investigaciones Científicas

Abstract

Formation Flying (FF) offers space-dependent disciplines such as astrophysics, astrodynamics, and geodesy, to name a few, the possibility of creating large spaceborne sensors from an array of small spacecraft flying in formation. This creates exciting scientific and technical opportunities as the formation could be arranged to work as, for example, an interferometer of essentially unlimited angular resolution or a virtual telescope of unrestricted focal distances. The definition of suitable algorithms for navigation and control of FF missions has become one the major challenges to realize full FF capabilities following the first validation of FF technology on NASA's New Millennium Program Earth Observing One (EO-1).

The focus of this dissertation is the design and evaluation of algorithms for navigation and control for formation flying missions. Given its importance, extensive research has been already conducted to fulfill the increase of accuracy, autonomy, and other requirements of the Guidance, Navigation, and Control (GNC) systems that derive from novel applications of formation flying missions. To center the scope of present work, we have mainly focused in three of the present challenges: the difficulties of fusing different non-linear observations for relative navigation; the analysis and extension of behavioral algorithms for controlling a formation of spacecraft; and the design and validation of a control law for formation acquisition and formation keeping of a non-natural relative trajectory. These three interconnected topics cover a wide range of research in formation flying and embody the main algorithm components of formation flying algorithms from the observations to the navigation and to the control.

The first challenge consisted, thus, in addressing the difficulties encountered by classical filters to estimate a state vector fusing common observations. We proposed several strategies to improve the robustness of these filters under non-linear conditions. Among these strategies, the modification of the residuals computation for the

Unscented Kalman Filter (UKF) deserves special mention due to its excellent results and robustness against nonlinearities. A theoretical basis for these results became, thus, necessary regarding the new update equation of the UKF and has been developed subsequently in the frame of this thesis. This work has been published in Perea et al. [36] and Perea and Elosegui [34].

The collective motion exhibited by some groups of animals has recently attracted the interest of many research groups who try to take advantage of the robustness and efficiency of natural patterns. With this aim, we have investigated the possibility of extending an interaction model that has shown emergent behavior. In particular, the Cucker-Smale (CS) model has been extended for its application on spacecraft formation flying. Numerical simulations of the Darwin mission have proved that this strategy is suitable for loose formation keeping. Of special relevance is the low cost of the controller, specially compared to an alternative strategy, the Zero Relative Radial Acceleration Cones (ZRRAC) [35].

The problem of tight formation keeping is addressed in [33] and [32]. In these papers, we first study the relative dynamics of a virtual telescope that follows a non-natural relative trajectory driven by the position of an observed body and not by the natural forces in space. This analysis has originated the design of several controls based on different approximations of the relative dynamics. Their performances have been tested and compared through numerical simulations of the PROBA-3 mission using, first, computer based simulations, and then, a realistic platform with GNSS hardware and operational flight software in the loop. The main conclusions show that simple control definitions, as defined by the Linear Quadratic Regulator (LQR) and Linear Quadratic Regulator with the Integral term (LQRI), can fulfill stringent requirements for formation acquisition and tight formation keeping.

Chapter 1

Introduction to study

1.1 Formation Flying Mission Definition

A Formation Flying (FF) mission consists of a set of two or more spacecraft whose dynamics is coupled through a common control law. This control law is usually expressed in terms of a relative state vector, which commonly includes relative positions and velocities, although some degrees of freedom can also account for rotational and translational displacements. It is quite common to incorrectly associate satellite constellation missions, such as Global Positioning System (GPS), with FF missions. However, the states of a constellation are not coupled in any way, and the orbit corrections for each spacecraft only require individual satellite state vectors. Indeed, the control law of a FF mission has to, directly or indirectly, consider the relative positions of the entire formation. This does not mean that all satellites need to feature an active control law, but, in that case, the control active satellites must track the inactive ones, or a target that depends on their positions. In case of all satellites have an active control, they must cooperate to achieve a common target, which can be modified along the mission lifetime. These missions can feature the possibility to rotate, expand, contract, and/or re-configure according to new targets, and enable evolution to larger formations. [42]

FF missions have significant benefits compared to single monolithic spacecraft including the possibility of unprecedented high resolution for scientific applications, novel applications in space, a reduction of the size and weight of the spacecraft with its consequent savings in launch costs, a simplification of spacecraft design, and the possibility of a fast replacement and redundancy in case of failure [9, 13].

1.2   Past, Present and Future of FF Missions

Earth Observing One (EO-1) was the first mission selected by National Aeronautics and Space Administration (NASA) in 1996 which considered FF technology[47]. Since then, dozens of missions involving FF technology have been proposed to NASA and other space agencies worldwide, considered, and moved throughout or up to various phases, including launch and operations. Some outstanding examples because of its scientific and technology outcome are the Cluster mission, to study Earth's magnetosphere using four coordinated satellites [12], and Gravity Recovery and Climate Experiment (GRACE) tandem mission, where the variations of the relative positions of its two satellites are used to study Earth's gravity fiels [45].

The expected outcome of proposed missions is evaluated against its risks before selection, taking also into account global policies of the agencies, and other economical aspects. Although some of the investigated missions are finally discarded for technical, scientific, economical, or even political reasons, the outcome of their preliminary feasibility studies and designs can be of great relevance for other FF mission technologies and applications. In this framework, some missions should be highlighted, such as DARWIN [51] and SIMBOL-X [53, 54], that have been cancelled during the realization of this thesis. The first one consisted

Figure 1.1: Artist impression of GRACE, DARWIN, and PROBA-3 missions, respectively. Source: NASA, ESA, and ESA, respectively.

in a formation of three to five satellites in an orbit around the second Lagrange point (L2) with the aim of identifying Earth-like planets with possibility of life, which presented several technological and scientific challenges. Before cancellation of this program, this mission was used as a reference scenario for the validation of novel control algorithms during the realization of present thesis. In turn, SIMBOL-X was envisaged as an X-ray telescope for investigating high-energy astrophysics. The telescope consisted in two satellites over a High Elliptical Orbit (HEO) with small inclination.

Table 1.1: Overview of future FF missions [18]

Mission	Launch Date	Number of Spacecraft	Main Field	Agency
TerraSAR-X and TanDEM-X	2007-2010	2	Earth's digital model and SAR interferometry	DLR/Astrium
PRISMA	2010	2	FF and Rendezvous (RdV) technology demonstration	SSC/DLR/ CNES/CDTI
PROBA-3	2012	2	FF and RdV technology demonstration	ESA
MMS	2013	4	Science. Magnetosphere	NASA
TPF	2015	4 or 5	Sub-mm telescope	NASA
PEGASE	2017	3	Infrared Interferometer	CNES
MAXIM	2020	34	X-ray telescope	NASA
MSR	2020+	2	Mars exploration. Autonomous long range RdV	ESA
LISA	?	3	Laser interferometer	NASA
JC2sat	?	2	FF and technology demonstration	CSA/JAXA

Groups of satellites are currently designed to build large synthetic aperture radars, which significantly improve the angular and spatial resolution of past monolithic space missions with several scientific applications. Table 1.1 contains an indicative list of envisaged FF missions, which has been built from [18, 27] and the latest updates in the webs of space agencies. Relevant examples of future applications because of its demanding technological and scientific challenges are Laser Interferometer Space Antenna (LISA) and Micro Arcsecond X-Ray Imaging Mission (MAXIM). LISA is intended to use large synthetic aperture technology to detect gravitational waves from a set of three coordinated satellites that will constitute a virtual telescope orbiting around the Sun, similar to Earth [10]. In turn, MAXIM will offer the possibility of observing the region bordering black holes, known as the event horizon, with unprecedented angular resolution [16] with a set of up to 34 satellites.

Another important set of missions comprise the technological ones. Before the investment on very challenging scientific missions with a technology demand well beyond the current state-of-the-art, some intermediate missions shall validate improvements on these technologies and be a leap between present and future space missions, such as

PRISMA [37], and PROBA-3 [49]. The principal aim of the PRISMA is to test and validate critical technologies related to advanced FF and In-Orbit-Servicing. Similarly, PROBA-3 will be a step forward in the demonstration of the novel technologies required for FF, in particular, the autonomy of Guidance, Navigation, and Control (GNC) systems, as the third mission of the ESA's Project for Onboard Autonomy. This last mission has been of special relevance in the frame of this thesis since it has been also used as a reference scenario for the development of some control algorithms, as it will be afterwards detailed.

1.3 FF Technology Roadmap

The present mission roadmap illustrates a constant increase in FF technology demands. The roadmap for achieving these technological challenges is, however, changing, and depends on the success for achieving a diversity of intermediate targets. Although the schedule and details of present technological roadmap for positioning and autonomy are unknown to the author, the reader may appreciate some notes. According to main space agencies, the control performances should reach the cm level in the next few years, and the nanometer (nm) level in approximately one decade [27, 39]. Obviously, the achievement of this accuracy would depend on the improvements in the navigation system, which were intended to reach the nm in approximately one decade, while accuracy of present operating missions is at the m level. Another significant challenge for the next decade is autonomy. Satellites are currently monitored and controlled mainly from ground control centers. Increasing autonomy would imply a reduction of the Earth-spacecraft communication links, an improvement on the control performances, and a prompt reaction to contingencies, such as impending collision. With this aim, several levels of autonomy have been identified for the flight Software (SW), fault detection and isolation systems, planning and scheduling systems, communications, etc.[27, 39]

The main technological areas under investigation for coordinated satellite missions can be summarized as follows:

Trajectory optimization; The design of trajectories must be optimized to reduce the cost of the control and maximize the scientific outcome during the lifetime of the mission.

Metrology; New sensors and instruments are under investigation and development for high accuracy, with special focus on autonomous systems and relative navigation.

Navigation and control algorithms; Novel algorithms are currently investigated to provide unprecedented high accuracy for relative navigation. Distributed spacecraft algorithms are also desirable to efficiently allocate the computational load, and the fuel for maneuvers among different spacecraft; and for robustness against failure of an entire satellite.

Actuators; High precision actuators have to be built to keep tight formations along large periods of time. Special focus of this development are electric and cold gas propulsion systems for formation keeping maneuvers.

Autonomy; One of the more challenging characteristics of the future coordinated satellites missions is autonomy. Increasing autonomy, and reducing ground monitoring tasks, would imply a reduction of the Earth-spacecraft links, an improvement on the control performances, and a prompt reaction to contingencies. With this aim, research has been also carried in the fields of guidance, navigation and control autonomy.

Communications; In order to reduce the satellite communications with ground control centers, the monitoring of the formation must be transferred to the formation for self-monitoring as much as possible. With this aim, suitable cross-link and protocols have to be designed for inter-vehicle communications.

Tools; Several tools & testbeds need to be developed to validate both the Hardware (HW) and SW before the launch of the mission, specially those FF specific issues.

Other; Other areas of research include mission planning, fault detection and isolation algorithms, nanotechnology, etc.

This thesis focuses on the navigation and control algorithms of a GNC system with special attention to autonomy. A GNC system is mainly in charge of providing answers for "where the satellite should be?," "where it really is?," and "how to go?,"

respectively. With this aim, several units must interact, such as the metrology, the GNC, and the propulsion systems.

The metrology system consists of a set of sensors that provide observations of the system, as inputs to answer the "where" questions. The navigation system processes these observations through a filter according to some physical models, which provides an estimation of the state vector within a certain accuracy. Then, the control algorithms must plan maneuvers scheduled according to the answers of the guidance and navigation systems. Finally, the actuators are in charge of executing the maneuver commands.

To focus the scope of present work, we have mainly focused in three of the present challenges involving the GNC systems. The first challenge addressed in this dissertation deals with the possibility of fusing inertial and relative observations in the navigation system, while the other two mainly deal with the definition of novel control algorithms exploiting the benefits of natural behavioral models and the design of simple algorithms to fulfill demanding positioning requirements, respectively. We describe these challenges in turn.

1.4 Navigation challenge

In the case of single satellite missions or constellations, the metrology system usually provides inertial observations only, i.e., inertial pseudo-range distances between each spacecraft and some Earth stations, or GPS satellites in case of GPS navigation. A new possibility of combining different types of observations frequently arises in case of coordinated satellites. In this new scenario, mainly absolute and relative pseudo-distances might be fused. Under these conditions, the most commonly used filters may provide a misleading estimation of the satellite location. [21]

A filter is a process to estimate the state vector of a system based on the set of available observations. As an example, for offline estimation of the mean orbital elements where all observations are available at a time, a Least Squares Filter (LSQ) could be used. However, this filter would not be used for real-time estimation, where the estimates for the orbital elements are updated after every new observation set is available. In this case, a sequential filter would be used instead. The Kalman Filter (KF) is the best known among them.

This filter, named after his author Rudolf E. Kalman, was first developed in 1960[24]. Since then, the KF and its version for nonlinear systems, the Extended Kalman Filter (EKF), have been widely used and discussed in estimation problems, specially in navigation, and they have become the most popular sequential filter[29]. However, the KF was designed under hypotheses of linearity and Gaussianity of the noises that can not be guaranteed in many situations, and it is the case when inertial and relative distances are fused. To overcome these limitations, several variations of the filter have been developed. Among them, the best known are the already mentioned EKF, the Iterative Extended Kalman Filter (IEKF), and the Unscented Kalman Filter (UKF). A parallel approach to designing variations of KF include the development of high-order filters such as the Gauss Second-Order Filter (GSF).

The difficulties associated to the estimation of a state vector fusing different sensors have lately received special attention. As previously mentioned, the possibility of fusing different kinds of observations, e.g., inertial and relative distances is of special interest for FF navigation. In such a metrology system, it is expected that the noise level for the relative observations is lower compared to the inertial observations. This feature, together with the nonlinear characteristics of the observations with respect to the state vector, have been proven to lead the EKF to a misleading estimation[21, 28, 38]. One of the main topics of this dissertation is the study of the divergence process in these conditions, and the identification of possible variations that overcome the divergence problem while keeping the computational load reasonable for online and onboard computation.

In Perea et al. [36] the authors study the divergence process of the EKF in detail using numerical simulations. As alternative filters, the performances of the Modified truncated Second Order Filter (mtSOF) and the UKF are compared under the same numerical conditions with relatively poor results. Thanks to the analysis of the divergence process, a new formulation for the UKF is suggested, and numerically compared to previous filters with excellent results.

1.5 Control challenges

During last thirty years, different strategies have been investigated and developed to fulfill the wide spectrum of FF control needs. Different control modes are usually iden-

tified for each mission: formation acquisition, formation keeping, collision avoidance, relocation, orbit escape, etc. and are usually fulfilled assuming different strategies for each control mode [26].

The fuel availability in space is a very limited good and the optimization of its consumption is one of the drivers in the design of suitable control algorithms. The first step for this minimization consists of trajectory optimization (see [44, chapter 5] for an introduction to the problem and [31] for an example) and the design of passive controls as long as they are feasible (e.g., [22]). The optimization consists of designing a trajectory to optimally perform the mission objectives, and it is usually solved by an application of the Hamiltonian-Lagrange theory, also referred to as calculus of variationals. In case active controls are also necessary, for instance for an orbit escape maneuver or formation reconfiguration, additional algorithms are required.

Traditional control schemes usually make direct or implicit use of Lyapunov control theory to guarantee convergence and they frequently consider natural or artificial potential functions, sometimes referred to as cost functions, to fulfill additional control requirements[43, 30]. These strategies can reach different levels of sophistication depending on the approximation for the spacecraft dynamics and the consideration of additional constraints, optimization criteria and adaptability performances.

New trends in the control theory consider models of emergent collective behavior for its application in space[41]. The natural aggregation and pattern formation processes shown by some biological groups, from bacteria to herds through insects, schools, and flocks, have been widely studied and applied in biology, robotics, economy, computer science and, quite recently, in space missions [46, Chap. 10: Swarms in Space Missions]. These novel strategies have been considered in this dissertation as a potentially powerful application. In Perea, Gómez, and Elosegui [35], the authors extend a control model first inspired by bacteria interactions in [48], lately generalized in [23], and extended to smoother interactions by Cucker and Smale [8], with excellent results.

This model is based on the cancelation of the relative velocities and acceleration based on the observed dynamics of the neighbor satellites. This strategy, referred to as Cucker-Smale (CS) after its authors in the dynamic-free environment, has been shown to provide reasonably good performances for loose formation keeping. A loose formation is when the position requirements of each spacecraft in the formation allow a significantly large range of locations. This is the case, for instance, of a group of

satellites in a transfer orbit that have to acquire a specific formation along the target orbit, but with no additional formation requirement during the transfer. As an example, the currently withdrawn mission DARWIN was conceived as a group of three to five satellites that should form a virtual telescope over a halo orbit around L2. One of the deployment options under consideration was to separate the satellites before the transfer and keep them in loose formation until the arrival to the halo. This scenario, indeed, have been the one used to test and compare the performances of the CS control.

An operation mode more characteristic of FF missions is the tight formation keeping mode. With the aim of building virtual telescopes from spacecraft formation, the relative positions must be controlled with high resolution, sometimes, along a non-natural relative trajectory [49]. For this purpose, the cancelation of relative dynamics and accelerations due to CS control may not be enough, specially in a Planetary Orbital Environment (POE), where there exist significant forces and environmental disturbances. The navigation errors, mismodeling inaccuracies, and hardware limitations may lead to a rapid violation of the tight formation requirements when using that control.

Most of the research performed for formation keeping in POE is based on the maintenance of a periodic solution of the relative dynamics[42]. Different approximations are usually considered to find stable solutions depending mainly on the eccentricity of the formation reference orbit. The better known and more commonly used are the Hill-Clohessy-Wiltshire (H-C)[3] and the Yamanaka-Ankersen (Y-A)[50] equations for circular, and elliptic orbits, respectively. On the other hand, there are other mission scenarios where the reference trajectory for a relative motion is not defined by a solution or approximation to the natural relative dynamics but by an external condition. This is the case of a virtual telescope that has to be aligned with a target body to collect observations. This dissertation is also devoted to this problem. In Perea, D'Amico, and Elosegui [33], linear and nonlinear approximations for the relative dynamics where considered in the design of three different control laws for tight formation keeping of a virtual telescope observing the Sun corona. According to the main results and conclusions of that study, an accurate control scheme have been designed afterwards for formation acquisition and keeping scenarios of the PROBA-3 mission in Perea et al. [32]. In that last work, two slightly different control algorithms are designed based on the solution of the Linear Quadratic Regulator (LQR) problem, one for formation

acquisition and the second one for formation keeping. The resulting scheme has been tested and validated with a GNSS hardware-in-the-loop FF platform.

1.6 Darwin and PROBA-3 missions

As part of the design and evaluation process of previous algorithms, two missions have been considered and used to define reference scenarios: Darwin and PROBA-3. Although these missions have been briefly introduced in the appended papers and the corresponding summaries (chapter 2), this section presents an extended overview to provide a global framework of the relevance of these missions. In the next sections, we introduce the main objectives, architecture, and the scenario of each mission.

1.6.1 Darwin

The FF Darwin mission was a first studied by European Space Agency (ESA) between 1997 and 2000, and became a relevant component of its Cosmic Vision 2020 Program since it was interrupted in 2007. Since then, no further activities have been planned for the future.

The principal aim of Darwin was to build an InfraRed Space Interferometer to search for Earth-like planets around other stars, analyze their atmospheres for chemical signatures of life, and to provide imaging of astrophysical objects with unprecedented spatial resolution.

Figure 1.2: Artist impression of DARWIN. Source: ESA.

This mission was, therefore, named after the English naturalist Charles Darwin. This scientist became famous for his theories on evolution and the natural selection that result in a revolution of life and natural sciences. Identifying exo-planets with signs of life might have significantly contributed the investigation of the evolution of galaxies, which deserved the name of Darwin mission.

Darwin would have consisted of three or four satellites that would have carried 3-meter diameter telescopes, plus the central hub spacecraft operating as a light collector.

The technology for the telescopes was based on the nulling interferometry with observations in the mid-infrared. The selection of these wavelenghts mitigates the onerous task of searching light from exo-planets that orbit stars, whose light may easily outshine the planet's light.

The infrared light has the particularity that it is partially absorbed by some gases and other substances strongly related to the existence of life, also referred to as biomarkers, such as carbon dioxide, methane, and water. The spectrometer onboard Darwin would have allowed the identification of these fingerprints from extra solar planets.

Launched with a Soyuz-Fregat rocket, the constellation would have orbited the libration point L2 of the Sun-(Earth+Moon) system, which is 1.5 million kilometers from Earth in the opposite direction of the Sun, thus, the Earth permanently projects its shadow at this point. An orbit around this point would have optimized the Darwin light conditions for space observation.

The propulsion system of the spacecraft would have probably consisted of tiny and highly-efficient ion engines, which only need five kilograms of fuel to last the entire five-year mission. These engines attain satellite movements by expelling, in the opposite direction, small particles at very high velocity.

The metrology system of the constellation was of special relevance due to its stringent requirements. In order to operate as a synthetic aperture telescope, the spacecraft must have been arranged with the millimeter level at typical baselines between 40 m and 1 km. Different metrology systems were considered to cooperate during different mission phases. These systems mainly encompass a FF Radio Frequency (RF) system, similar to GPS, and optical observations.

Although extensive research and development was carried on in fields of nulling interferometry, metrology, FF technology, and validation platforms, the demanding requirements of this mission could not be fully validated when it was cancelled in 2007. Additional investigation would have been necessary to successfully prove its feasibility.

1.6.2 PROBA-3

The PROBA-3 mission is the next step in the General Support Technology Programme (GSTP). The GSTP is aimed at consolidating promising engineering concepts and readying for final space application with special focus on in-orbit demonstration. This demonstration is usually performed on carriers of opportunity, such as the International

Space Station, or through dedicated space missions consisting in small and cheap satellites such the Project for Onboard Autonomy (PROBA) satellites.

In this context, two PROBA missions precede PROBA-3. The objectives of the single satellite mission PROBA-1 were to demonstrate and evaluate new HW and SW spacecraft technologies, onboard operational autonomy, and Earth observation and space environment instruments. This mission was successfully launched in October 2001 and it is still operating as Earth Observation Third Party Mission. PROBA-2, in turn, consists of a single satellite that should validate several new technologies such as a dual-frequency GPS receiver, a xenon gas propulsion system,

Figure 1.3: Artist impression of PROBA-3 mission. Source: ESA.

and new GNC algorithms, among many others. The PROBA-2 was launched in November 2009 and the commissioning phase was planned to take approximately two months, thus, it is expected to become soon operational.

PROBA-3 is intended to in-orbit validate FF techniques and technologies with the scientific aim of observing the Sun's corona, as part of the FF demonstration, during a mission lifetime of 2 years. The main technological objectives include the validation of GPS and RF-based relative positioning navigation systems, new optical metrology systems, formation acquisition and keeping capabilities, and collision avoidance algorithms.

This mission will consist of a pair of satellites that should constitute a virtual telescope along a HEO. Named occulter and coronagraph after their scientific payload, the satellites should keep a baseline separation of 150 m during Sun observations, and they should be permanently aligned with the Sun.

Two candidate orbits were preliminary considered with orbital periods of 24 h and 72 h, respectively, being the first one finally selected for PROBA-3. In order to avoid excessive fuel consumption to keep the formation during the perigee, the operations requiring tight formation keeping will be limited to the apogee passage. During the perigee passage, the spacecraft should keep a safe separation in free flying mode and perform collision avoidance maneuvers if necessary. After that, the formation should be acquired and kept in coarse mode. Along the apogee passage, the formation should keep tight formation for Sun observations or it should perform a series of precise FF

demonstration maneuvers, including rotation, resizing, and maintenance. Figure 1.4 sketches the different orbit passages.

The metrology system for relative navigation will mainly comprise three different equipments: a Formation Flying Radio Frequency (FFRF) metrology system (similar to GPS), an optical Coarse Lateral Sensor (CLS) and an optical Dual Wavelength Interferometer (DWI) which incorporates a Fine Lateral Sensor (FLS). Additionally, GPS receivers should provide absolute position close to the perigee. Star tracker sensors should also significantly contribute to the attitude determination. The successful demonstration of these metrology systems will be regarded as a significant step forward in the FF missions roadmap.
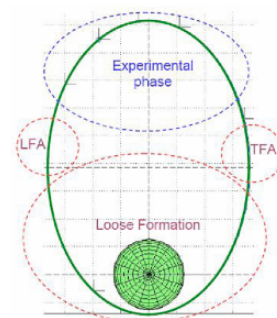
Figure 1.4: Orbit passages scheme. Source: ESA.

During the FF experiments, the occulter spacecraft is assumed to be passive, i.e., with no active control, and the coronagraph is in charge of achieve the formation requirements. With this aim, electric propulsion micro thrusters have been envisaged onboard the coronagraph. The impulsive collision avoidance maneuvers require higher thrust and have been allocated to a cold gas propulsion system onboard the occulter. Additionally, reaction wheels and attitude control actuators have been also envisaged for both spacecraft.

After the industry early studies for PROBA-3 were initiated in 2004, the mission Phase A was successfully conducted and finalized in 2007, and the mission is currently in its Phase B. Once the subsequent Phase CD is completed, the two satellites are expected to be mounted on a Vega launcher and lifted off in mid-2012.

1.7 Thesis Outline

This dissertation is presented as a compendium of the papers that have been published or submitted for publication in international journals or in conference proceedings as part of my PhD research. The content has been organized as follows. Chapter 2 contains a summary of these publications. The main conclusions and outcome has summarized in Chapter 3. Next chapter 4 includes a summary of this dissertation in my native language, catalan. The previously cited manuscripts are collected in Appendix A and

sorted in chronological order. Finally, a list of the coauthors of the works has been also included in Appendix B including their affiliation. The bibliography, nomenclature and a list of acronyms can be found at the end of the dissertation.

Chapter 2

Summary of appended papers

Much of the graduate work performed in the course of this research period has already been published or submitted for publication, as proceedings and journal papers. This chapter is thus devoted to contextualize and summarize those publications. A separate section has been assigned to each paper following the chronological order of publication. A copy of the original papers can be found in Appendix A. A list of the coauthors together with their affiliation have been included in B for reference.

2.1 Nonlinearities in Sensor Fusion: Divergence Issues in EKF, Modified Truncated SOF, and UKF

This section summarizes the contents of the work by Perea et al. [36], which was presented at the AIAA Guidance Navigation and Control Conference and Exhibit in 2007, and published as part of the conference proceedings.

As already introduced, the relative navigation of collaborative spacecraft brings the possibility of fusing different kind of observations, notably inertial and relative distances. Fusing different sets of observations is very desirable in any experimental endeavor because it can help improve the accuracy of the state estimations specially when the observations add not only redundancy but also complementarity. However, fusing observations has been shown to be challenging since the fusion can result in misleading estimations in a significant set of scenarios. This is the case when the magnitudes of the second-order terms of the observation models (with respect to the

state vector) are significantly different among the different types of observations, and the ones with larger second-order terms are the ones with higher accuracy. As shown in [21, 28, 38], these conditions can lead the EKF, which has has been commonly used for space navigation, to divergence.

In the present work, the divergence process of the EKF is analyzed in detail using numerical simulations. In order to isolate the difficulties associate to the observations with the difficulties associated with the time update, we considered the problem of estimating the relative position of a static formation using angle and distance observations. As representative of state-of-the-art sensors, we assumed that the angle observations are significantly more accurate than the distance samples. According to the step-by-step analysis, the filter seems to diverge due to an overestimation of the linear models of the observations. The uncertainty on the state estimation is updated based on a constant approximation of the observation models and completely neglects any information from the residuals. Thus, the filter shows a discrepancy between the speed of convergence of the state estimation and the uncertainty matrix. This, in fact, leads to a misinterpretation of the new observations and results in an estimation with a large error and an associated uncertainty matrix excessively small, which has been referred to as filter divergence.

Common alternatives to the EKF are the mtSOF and the UKF. For an easier comparison of the formulation of these filters, a common expression has been provided for all these filters. Although the results of these alternative filters generally improve with respect to the EKF the results are generally poor for this problem, and frequently yield to divergence. Thus, some modifications or alternatives become necessary even for these filters.

With the aim of preventing the uncertainty matrix to shrink excessively quick, several bump-up strategies have been proposed in this work to modify the previous filters and account for the mismodeling effects of the observations. These strategies have been mainly borrowed from previous works of Plinval [38], and Mandic [28], and references therein, and significantly improve the performances of the original filters.

The step-by-step analysis of the UKF divergence process also suggested that there was some useful information in the observations that was underused due to the definition of the residuals in the UKF. This result indicated that a new definition of the residuals could lead to a significant improvement of the performances. The numerical

comparison of this modification, referred to as Unscented Kalman Filter with residuals modification (UKFz), with respect to previous filters and bump-up strategies showed that this new formulation outperforms all previous algorithms providing excellent and robust results.

The paper also provides a sensitivity analysis of the filter performances with respect to the different variables that are involved in present example (observation noise levels, the initial error, and the initial state uncertainty). The main result of this extensive comparison was that the UKFz clearly outperforms all previous filters in most of the configurations with no additional cost in terms of computational load, compared to the UKF.

In conclusion, we have successfully identified and designed different strategies to improve the performances of the EKF, and the UKF for data fusion. In particular, these variations of the classical filters should result in a significant improvement of the navigation estimations in FF missions. Further research should address the numerical performances of the Improved Unscented Kalman Filter (IUKF) under a realistic FF scenario compared to classical filters.

2.2 New State Update Equation for the Unscented Kalman Filter

This section summarizes the contents of the work by Perea and Elosegui [34], which was published in the Journal of Guidance, Control and Dynamics in 2008.

The motivation of this work was to develop the theoretical foundation to prove the validity of the novel UKFz formulation proposed in previous paper (Perea et al. [36]). Based on the excellent numerical results that the UKFz showed, a new definition for the UKF residuals was foreseen as more robust and powerful against general non-linear problems.

In this work, we develop the theory that supports a new formulation for the UKF that incorporates this new definition of the residuals. Although the resulting filter, named IUKF, is slightly different from the original UKFz, the UKFz has been also justified since it consists in a bump-up of the IUKF.

The aim of this paper is, thus, the presentation of a new state update equation for the UKF based on a novel definition of the residuals, which implicitly incorporate second-order information of the state errors. For this derivation, the UKF is first introduced and its underlying assumptions are made explicit. This filter borrows the formulation of the EKF and makes advantage of a more powerful strategy for the computation of uncertainty matrices, namely the unscented transformation. In the same way, the state update equation of the IUKF is built as a first order polynomial of the new residuals while taking the same advantages of the unscented transformation of the UKF. The different assumptions and approximations that are considered in the definition of the polynomial coefficients have been proved to have an error, at least, comparable to the error of the UKF. However, the implicit inclusion of high-order terms in the residuals results in a significant improvement of the filter performances.

The numerical performances of this new formulation have also been presented in this work for the same example and baseline configuration used in [36], which is representative of the difficulties experienced in formation flying sensor fusion.

2.3 Extension of the Cucker–Smale Control Law to Space Flight Formations

This section summarizes the contents of the work by Perea, Gómez, and Elosegui [35], which was published at the Journal of Guidance, Control, and Dynamics in 2009.

As previously introduced, the emergence of group behavior shown by swarms has recently caught the attention of research groups in space engineering (e.g., [41]) as a source of promising algorithms for formation control. In this paper, we extend a behavioral model, first developed by Cucker and Smale in [8], to space flight formations for formation acquisition and loose formation keeping.

The CS model was first inspired by the emergence of self-ordered motion shown by a group of biological particles that, with constant velocity, modify their individual headings with the average heading of particles in neighborhood [48]. Instead, the authors of [8] proposed an interaction model where each individual modifies its velocity with a weighted average of the relative velocities with respect to the rest of individuals

in the complete group. In this case, the weights depend on the relative distance between two individuals, which may account for the larger uncertainty naturally associated to the knowledge of relative position and velocity of faraway individuals than nearby. Thus, the velocity of neighbors in the close vicinity of an individual modify its velocity more intensively than other individuals.

In that work, the authors provided a specific formulation of the weights for the velocity average and a characterization of the specific conditions that should verify certain configuration parameters to guarantee the emergence of collective motion. Indeed, the authors prove that, under certain conditions, the swarm will finally move as a rigid body with constant velocity, and would not split into smaller groups of individuals.

In [35], we provide an extension of this model to the space realm by modifying the velocity of a spacecraft with the relative acceleration with respect to the geometric center of the formation and the weighted average of the relative velocities according to the CS model. Based on the results of Cucker and Smale, we directly derive a characterization of the involved parameters to guarantee that the initial group tends to move as a rigid body with the dynamics defined by the geometric center of the satellite formation.

An extensive discussion is also provided regarding the parallel computation and inter-vehicle communication needs associated to this control algorithm. Possible limitations of the control system are also envisaged and discussed, such as discretization of the control actions and maximum and minimum thrust capabilities.

In order to test the performances of this control algorithm, we considered the Darwin mission as a reference scenario. In particular, the performances of the CS control where evaluated along the transfer trajectory of three spacecraft from an Earth orbit to a halo orbit around the libration point L2 of the Sun-Earth system since one of the formation deployment options first envisaged for Darwin consisted in transferring the three spacecraft separately along the transfer orbit and keep them in loose formation meanwhile.

An extensive sensitivity analysis of this control algorithm has been carried on using numerical simulations. The different configuration and initial parameters that are involved in the control algorithm and mission scenario have been identified and several simulations have run to address the algorithm sensitivity on each one of these parameters. The performances of the control, under these simulations, have been evaluated

based on two indicators: the maximum separation from the reference trajectory, and the total Delta v, or fuel expenditure.

For comparison purposes, we also considered the numerical results in Gómez et al. [17]. In that paper, the authors present a novel strategy based on the existence of certain cones around the transfer orbit with their centers on the reference trajectory and with the characteristic that the relative radial acceleration along the generatrices of the cones is zero. This strategy, referred to as Zero Relative Radial Acceleration Cones (ZRRAC) control, was also tested using numerical simulations of the Darwin transfer orbit for formation keeping purposes.

The numerical simulations showed the importance of a good tuning of the configuration parameters of the CS control algorithm. Thus, the optimum configuration parameters have to be selected based on the specific mission characteristics, mainly the range of possible initial relative velocities, and the maximum time between consecutive maneuvers. Under the optimized values, the CS algorithm provided minimum variations of the initial relative distances at the same time as the fuel expenditure is minimized. The algorithm has been also proved to be robust against noises on the navigation data (position and velocity), which have been tested as part of the mission scenario parameters. Finally, comparison between the CS and the ZRRAC numerical simulations, whenever possible, have shown that the first one significantly reduces the fuel expenditure while providing similar, or even smaller, variations of the inter-vehicle separations than the ZRRAC.

In conclusion, the CS control algorithm has been shown to be suitable for formation acquisition, and loose formation keeping along a transfer orbit. However, the area of application of this strategy is not limited to these kind of orbits but it can also be considered in deep space, where the disturbance forces are minimum. The suitability of this strategy in POE could be a topic of further research, with special focus on the comparison of performances of the control against the altitude of the spacecraft.

2.4 Relative Formation Flying Dynamics and Control of a Two-Element Virtual Telescope on a HEO

This section summarizes the contents of the work by Perea et al. [33], which was presented at the 21st International Symposium on Space Flight Dynamics in 2009, and

published as part of the conference proceedings.

In paper [35], we have presented a control algorithm for formation acquisition and loose formation keeping based on a behavioral model. However, this algorithm may not be suitable to acquire a specific formation since the CS control does not guarantee a final configuration. Once the formation is acquired, the CS control might be used to keep it as a rigid body. In order to follow a specific reference trajectory, the coordinate system must be chosen in such a way that the relative positions are constant over the reference trajectories, which may lead to forced and complicated coordinate systems. Moreover, the mismodelling of the relative dynamics and hardware limitations may lead to a rapid violation to stringent formation requirements, which will probably make this strategy unsuitable for tight formation keeping.

This is the case, for instance of a virtual telescope that has to be perfectly aligned with the observed body. The principal aim of [33] is to design and validate a control algorithm for a virtual platform that does not follow a natural relative trajectory, as in PROBA-3 [49]. This mission is a technological mission that shall prove some of the novel technological improvements for autonomous navigation and control of a flight formation. As the main payload, the formation will carry an occulter and a coronagraph for Sun corona observations. With this aim, the two spacecraft that constitute this mission have to be aligned with the Sun.

The relative dynamics between the coronagraph and its reference trajectory directly depends on the Sun and occulter positions. In present paper, we first address the relative dynamics of a formation of two spacecraft at a baseline distance of 150 m along a HEO, as envisaged for PROBA-3. With this aim, we quantify the magnitude of the relative accelerations due to the different force sources, e.g., the Earth gravity, the oblateness of the Earth, and the Solar Radiation Pressure (SRP). Due to the different illumination conditions of the two satellites, one projects its shadow to the other, the two forces that drive the relative dynamics are the Earth gravity, and the SRP.

Based on the analysis of the relative dynamics, we propose three control laws for the acquisition and maintenance of the formation, that stem from different approximations of the relative dynamics. The first control mainly consists in two terms: the relative acceleration to cancel variation of the dynamics with respect to its reference and a

2. SUMMARY OF APPENDED PAPERS

linear term for formation acquisition. The relative acceleration is approximated by the two main forces, i.e., the Earth gravity and the SRP, while the linear term is defined by a Hurwitz matrix -with the poles on the left-hand side of the complex plane-. Since the approximation to the relative dynamics hereby considered is not linear, this control has been named as the nonlinear control in contrast with the other two.

Indeed, these two other controls are based on a linear approximation of the relative dynamics. Under this assumption, a feedback gain matrix is designed to guarantee that the real trajectory will tend to its reference. With this aim, we first address the approximations necessary to linearize the dynamics. As a result, the relative SRP is completely omitted in this approximation, as well as the constant component of the relative acceleration due to the Earth gravity. This approximation is then used to define two control functions that are linear in the error vector.

The robust pole-placement control considers the Kautsky-Nichols-Van Dooren (KNV) algorithm to compute the feedback gain matrix, while the LQR control additionally considers a cost function and designs the feedback gain matrix to minimize its value. These algorithms make use of some configuration parameters -the poles definition and the error and control weighting matrices, respectively- that need to be tuned for each specific problem.

The three controls have been compared using numerical simulations. As previously mentioned, we have considered the ESA mission PROBA-3 as a reference scenario in present study. More specifically, we have considered the experimental phase, when the formation has to be acquired for Sun corona observations and tightly kept along the apogee passage. Two HEO orbits have been simulated since both of them were preliminary under consideration when this research study begun [49]. These orbits have periods of 1 and 3 days, respectively, being the first one afterwards selected for PROBA-3 [40]. The specific characteristics of the orbit, experimental phase, and modes of operation are also introduced in this paper together with other relevant data for the definition of the scenario.

The experimental platform developed for testing and comparing the control laws is also fully described in the paper, including the dynamics, the metrology system for relative navigation, and the complete characteristics of the GNC models.

The significance of the tuning of each control algorithm is first introduced as part of the results. As explained in section "Results and Discussion", unsuitable values

may result in thruster saturation, slow convergence, or high frequency oscillations of the position error of the controller. Examples of these behaviors are provided for the nonlinear control. Furthermore, the role of the configuration parameters of each control is also discussed and compared among them, being the LQR the easier algorithm for tuning.

Under optimized configurations, however, all control algorithms provide similar performances and can reduce an initial position error with respect to the reference trajectory from several meters to the cm level, according to present simulations. The only remarkable difference consists in the error reduction when accurate models of the relative acceleration are considered within the control, as it is the case of the non-linear control. However, the inclusion of nonlinear components of the relative dynamics is only worth after formation acquisition and when the relative accelerations are sufficiently large, i.e., at relatively low altitudes. Otherwise, the error component linearly included in the control definition absorbs the mismodelling errors and yields all controls to provide similar performances.

2.4.1 Additional notes

Regarding the computation of the SRP that affect the coronagraph, the definition of the occulter shadow coefficient φ was not included in the paper and is developed here for completeness. Using the same nomenclature as in [33], it should be defined as:

$$\varphi(x_{cs}) = \frac{1}{|S|} \int_S \eta(x) dx \tag{2.1}$$

Now, equation (5) from reference [33] can directly be derived from

$$
\begin{aligned}
f_{SRP}(x_{os}) &\approx \nu(x_{os}) a_{srp}(x_{os}) \\
&= \nu(x_{os}) P_\odot A U^2 K_{os} \frac{x_{os} - x_\odot}{||x_{os} - x_\odot||^3}
\end{aligned}
\tag{2.2}
$$

and

$$
\begin{aligned}
f_{SRP}(x_{cs}) &= \frac{1}{|S|} \int_S \eta(x) a_{srp}(x) dx \\
&\approx \frac{a_{srp}(x_{cs})}{|S|} \int_S \eta(x) dx \\
&= \varphi(x_{cs}) a_{srp}(x_{cs}) \\
&\approx \varphi(x_{cs}) \nu(x_{os}) a_{srp}(x_{os})
\end{aligned}
\tag{2.3}
$$

Regarding the inclusion of the nonlinear components of the relative dynamics in the definition of the control algorithms, there are additional considerations that are worth noting. First, in the case of the contribution to the relative dynamics arising from the Earth's gravity, the larger nonlinear contribution consists in a constant term. Second, the largest nonlinear component of the SRP contribution is of second-order, and of lower magnitude than the Earth contribution -except at high altitude where the nonlinear terms play no significant role-. Therefore, the second-order terms due to variations of the SRP can probably be omitted from definition of the nonlinear control, and the relative SRP can be reasonably approximated (within the control definition) by a constant value along the reference trajectory. Thus, the nonlinear contribution can easily be limited to the inclusion of a constant contribution along the reference trajectory during formation keeping maneuvers. The inclusion of such a constant would allow an improvement of the performances similar to the results shown in the paper by the nonlinear control compared to the remaining controls at no additional cost in terms of computational burden.

2.5 Relative Control of a Virtual Telescope in High Elliptical Orbit using GNSS and Optical Metrology

This section summarizes the contents of the work by Perea et al. [32], which has been submitted for publication in the Journal of Guidance, Control and Dynamics in January 2010, as an engineering note.

In this paper, we further build on previous work and develop control strategies for formation acquisition and formation keeping of a virtual telescope that has to be aligned with the observed body, thus following a non-natural trajectory, taking as a reference the PROBA-3 mission. Based on the good performances of the LQR control, its simplicity of implementation, and the reduced computational cost onboard, we again consider it for formation acquisition. In order to reduce possible biases of the position error due to the controller at steady-state, we also present an extension of the LQR for formation keeping by including the integral of the error since steady-state. The resulting

control algorithm is referred to as Linear Quadratic Regulator with the Integral term (LQRI) and is designed for tight formation keeping.

These two control algorithms have been implemented in a formation flying platform for its validation under a realistic environment. We used the GSOC Formation Flying Testbed (FFTB), which was formerly designed and developed to test and validate the GNC algorithms for the PRISMA mission. This platform emulates the spacecraft dynamics and attitude, embeds the onboard GNC algorithms, and includes a Spirent GS7700 and two single-frequency Phoenix GPS receivers in-the-loop. For the validation of the present control scheme, we have also considered the navigation algorithms of PRISMA mission. This is also a technological mission aimed at validating sensor and actuator technology and demonstrating autonomous formation flying capabilities, and consists of two satellites flying in formation along a Sun synchronous orbit. The navigation algorithms for PRISMA process GPS observations for relative navigation, as envisaged for the PROBA-3 navigation at low altitudes, and have been reused in present simulations. Due to the significant differences between PRISMA and PROBA-3, some upgrades have been necessary.

A brief description of the FFTB and the navigation algorithms for PRISMA has been included in present paper providing some references for further reading. The necessary upgrades are described with more detail as it corresponds to a new contribution, including the simulation models of an optical metrology system for relative navigation at high altitudes.

As already stated, we again consider the PROBA-3 mission as a real example of a virtual telescope that has to be aligned with the Sun during the experimental phase. The mission characteristics, GNC system attributes, and modes of operation are briefly introduced, together with the configuration of the control algorithms, to describe the scenario for the simulations.

The performances of the complete GNC system are analyzed in detail along one orbital period, with the exception of a short interval along the perigee passage which is out of scope of this study. First, the performances of the relative navigation system are addressed using GPS and, then using the optical metrology system at higher altitudes. Second, the accuracy of the guidance system is also characterized, and finally, the performances of the control algorithms under formation acquisition and formation keeping modes are studied. As a global result, the interaction of the complete GNC

system allows a reduction of a position error with respect to its reference from 8 m to the cm level.

It is suggested, as a further work, to improve the accuracy of the relative velocity estimation when using optical observations to reduce the oscillations of the control input, and as a result, reduce the cost of the control. This can be achieved by improving the estimation filter of the optical navigation system.

In conclusion, we have developed a simple control algorithm and proved its validity for stringent control requirements. The simulations under the PROBA-3 scenario, must be considered as a realistic example, but the application of this technique does not limit to this mission and can be easily extended to other formations in POE. This results of special interest when the reference trajectory is defined by a non-natural trajectory.

2.5.1 Additional notes

The PROBA-3 scenario that we simulated follows the mission parameters as defined in [2, 49, 39]. Still, some of the key mission parameters such as the perigee passage and observation phase durations were not fully defined, thus, unavailable to us at the time of this research. Without lose of generality, we have considered values that we believe as reasonable. Any variation on these values will obviously result in a variation of the numerical performances, but the qualitative assessment that we have already presented should still be valid. Indeed, the modification of certain scenario conditions, such as the passage duration, and noise levels of the observations, among many others, should not yield to different conclusions regarding the suitability of the controls presented.

As an example of these parameters, we have assumed that the observation phase -almost equivalent to the passage with formation keeping control- takes approximately 22 hours while a recent document [40] limits its maximum duration to 12 hours. This limitation results in a reduction of the apogee passage which directly yields to a reduction of the cost of the control. Since the magnitude of the orbital perturbations decreases as the altitude increases, this might also result in a modest reduction of the position error on the control along the passage. However, no significant qualitative variations of the results would be expected compared to previous analysis.

Chapter 3

Conclusions

This research deals with the design and evaluation of algorithms for navigation and control suitable for formation flying missions. In particular, our interest has focused on the possibility of sensor fusion for relative navigation, the usage of behavioral models for formation control, and the control algorithms to keep non-natural relative trajectories.

Regarding the difficulties of fusing non-linear observations for relative navigation, the causes for filter divergence have been identified. According to [36], the discrepancy between the convergence speed of the state estimation and the speed for the uncertainty matrix leads the filter to a misinterpretation of new observations and results in filter divergence.

Based on this rationale, some bump-up strategies have been proposed which improve the performances of the classical filters. Additionally, a modification of the state update equation of the Unscented Kalman Filter (UKF) has been proposed, formally proved and numerically validated. According to the extensive simulation assessment performed, it provides robustness against nonlinearities and excellent estimations, outperforming all previous filters.

We have successfully extended a control model of swarms to spacecraft formation flying missions for formation acquisition and loose formation keeping. The convergence conditions have been theoretically identified and numerically validated using simulations of the Darwin mission. These simulations show that this control law can acquire and keep a formation with reduced variations on their relative positions at a cheap cost in terms of total Delta v, specially compared to the Zero Relative Radial Acceleration Cones (ZRRAC) control.

3. CONCLUSIONS

A simple linear design of a control has been theoretically developed and numerically proved to achieve stringent control requirements for formation acquisition and keeping of a formation of satellites that have to follow a non-natural relative trajectory with high precision.

Capítol 4

Resum en català

El vol de satèl·lits en formació ofereix a les disciplines de l'espai, com ara l'astrofísica, l'astrodinàmica i la geodèsia, per anomenar-ne unes quantes, la possibilitat de crear grans sensors espacials a partir d'un petit grup de satèl·lits en formació. Disposar els satèl·lits per a operar com, per exemple, un interferòmetre, i per tant, oferint una resolució angular gairebé il·limitada, o com a telescopi virtual i aconseguir distàncies focals inimaginables amb un únic satèl·lit, crea grans oportunitats científiques i tècniques. Des del moment en que la NASA va seleccionar la primera missió espacial que incorporava tecnologia de vol en formació (EO-1), un dels reptes que es preveien per a realitzar autèntiques missions de vol en formació és la definició d'algorismes específics per a la navegació i control dels satèl·lits.

L'objectiu principal d'aquesta tesis és el disseny i avaluació d'algorismes de navegació i control apropiats per al vol de satèl·lits en formació. Donada la importància d'aquestes missions, s'ha realitzat una extensa investigació per aconseguir acomplir amb l'increment d'objectius referents a la precisió, l'autonomia, i altres requisits del sistema de Guiat, Navegació i Control (GNC) que resulta de les noves aplicacions d'aquestes missions. El contingut d'aquesta tesis es centra en tres reptes actuals referents al sistema GNC: les dificultats de combinar diferents tipus d'observacions no lineals per a la navegació relativa; l'anàlisi i extensió d'algorismes de "comportament" per a controlar una formació de satèl·lits; i el disseny i la validació d'una llei de control per a l'adquisició i manteniment d'una formació en trajectòria no natural. Aquests tres temes interconnectats cobreixen una àmplia àrea de recerca en el camp del vol en formació i incorpora els principals components dels algorismes de vol en formació, des de

les observacions fins a la navegació i el control.

La majoria del treball realitzat durant aquest període de recerca ha estat publicat o està pendent de publicació dins les actes de congressos o en revistes internacionals. En les seccions següents es resumeix el contingut d'aquests articles en català per ordre cronològic de publicació. La còpia original dels articles es pot trobar a l'Apèndix A.

4.1 No Linealitats en la Combinació de Sensors: Problemes de Divergència Associats a l'EKF, al SOF Modificat i Truncat, i a l'UKF

En aquesta secció es resumeix el continut de l'article [36], que ha estat presentat al congrés AIAA Guidance Navigation and Control Conference and Exhibit l'agost del 2007, i publicat a les respectives actes.

La navegació relativa de satèl·lits en col·laboració ofereix la possibilitat de combinar diferents tipus d'observacions, típicament inercials i distàncies relatives. Combinar observacions provinents de diferents sensors resulta desitjable per tal de millorar la precisió de les estimacions, especialment quan les observacions incorporen no només redundància sinó també complementaritat. S'ha demostrat, però, que combinar observacions pot ser un repte real ja que aquesta combinació pot fer que es generin estimacions incorrectes en un gran nombre d'escenaris. Aquest és el cas de les combinacions on la magnitud dels termes de segon ordre dels models d'observacions (respecte al vector d'estat) son significativament diferents entre els diferents tipus d'observacions, especialment quan les que inclouen termes més grans de segon ordre son les més precises. Tal i com es demostra en [21, 28, 38], aquestes condicions poden portar al filtre extès de Kalman (EKF), un dels filtres més significatius en la navegació espacial, a divergir.

En aquest treball s'estudia en detall el procés de divergència de l'EKF utilitzant simulacions numèriques. Per fer-ho, hem considerat l'estimació de la posició d'una formació estàtica utilitzant mesures d'angle i distància. Tenint en compte les característiques dels sensors més avançats del moment, hem assumit que les observacions d'angle son força més precises que les de distància. D'acord a l'anàlisi seqüencial que presentem, el filtre sembla que divergeix degut a una sobreestimació dels models lineals

de les observacions. El grau d'incertesa de l'estimació (matriu de covariança) s'actualitza d'acord a una aproximació constant del model i omet completament qualsevol informació dels residuals. Així, el filtre mostra una discrepància entre la velocitat de convergència del vector d'estat i la corresponent matriu de covariança que porta al filtre a confondre la informació de les noves observacions i acaba resultant en la divergència del filtre.

Alternatives comuns a l'EKF son el filtre de segon ordre modificat i truncat (mtSOF) i el filtre "inodor" de Kalman (UKF). Per tal de facilitar la comparació de la formulació d'aquests filtres, l'article presenta una formulació comú. Tot i que els resultat generalment milloren quan es comparen amb els de l'EKF, aquests continuen sent pobres i, altra vegada, tenen tendència a divergir. Per tant, esdevenen necessàries alternatives o modificacions a tots aquests filtres.

Amb l'objectiu d'evitar que la matriu de covariança es redueixi excessivament ràpid, s'han proposat diferents estratègies d'explosió que modifiquen els filtres anteriors i tenen en compte els errors de modelatge de les observacions. La major part d'aquestes estratègies s'ha pres de treballs anteriors de Plinval [38], i Mandic [28], i les referències derivades, i milloren significativament les prestacions dels filtres originals.

L'anàlisi seqüencial de la divergència de l'UKF suggereix que hi ha informació útil en les observacions que es desaprofita degut a la definició dels residuals en l'UKF. Aquest resultat indica que una nova definició dels residuals pot donar lloc a una millora substancial dels resultats. La comparació numèrica d'aquesta modificació, anomenada com a UKFz, respecte els filtres anteriors i les corresponents estratègies d'explosió, mostren que aquesta nova formulació supera els algorismes anteriors i aconsegueix una robustesa i estimacions excel·lents.

L'artícle també ofereix un anàlisi de sensibilitat del filtre respecte a les diferents variables que estan involucrades en l'exemple actual (nivell de soroll de les observacions, error inicial, i matriu inicial de covariança). El resultat principal d'aquesta comparació extensiva ha estat que el UKFz clarament supera als anteriors filtres en la majoria de les configuracions sense cost addicional en termes de càlculs, comparat amb l'UKF.

Com a conclusió, hem pogut identificar i dissenyar amb èxit diferents estratègies per tal de millorar les prestacions dels filtres EKF, i UKF per a la combinació d'observacions. En particular, aquestes variacions dels filtres clàssics haurien de donar lloc a millores substancials de l'estimació relativa en missions de vol en formació. El següent

pas per a l'aplicació d'aquests filtres en missió espacial de vol en formació consisteix, doncs, en estudiar les prestacions numèriques de l'IUKF sota un escenari més realista i complert, tema que podria donar lloc a una futura investigació.

4.2 Nova Equació d'Actualització d'Estat per al Filtre In-odor de Kalman

En aquesta secció es resumeix el contingut de l'article [34], publicat a la revista Journal of Guidance, Control and Dynamics l'any 2008.

La motivació d'aquest treball ha estat desenvolupar la base teòrica per demostrar la validesa de la nova formulació UKFz que es presenta en l'article anterior ([36]). Partint dels excel·lents resultats numèrics que ha mostrat l'UKFz, proposem una nova definició dels residuals de l'UKF amb l'objectiu d'aconseguir un filtre més robust a les no linealitats de les observacions i que ofereixi millors estimacions que els filtres clàssics.

En el present treball, desenvolupem una nova formulació per a l'UKF que incorpora aquesta nova definició dels residuals. Tot i que el filtre obtingut, anomenat IUKF, és lleugerament diferent del filtre original UKFz, la validesa del filtre UKFz queda justificada ja que aquest consisteix en una explosió del filtre IUKF.

L'objectiu d'aquest artícle és, doncs, la presentació de la nova equació d'actualització per al filtre UKF basada en la nova definició dels residuals, que implícitament incorporen informació de segon ordre de les observacions. Amb aquest objectiu, primer introduïm el filtre UKF ressaltant les hipòtesis de que fa ús. Aquest filtre pren la formulació del filtre EKF i utilitza una estratègia diferent per al càlcul de les matrius de covariança del error, anomenada transformació inodora, i que resulta molt apropiada sota condicions de no linealitat. De la mateixa manera, l'equació d'actualització de l'estat de l'IUKF es construeix com a un polinomi de primer ordre en els nous residuals aprofitant les avantatges de la transformació inodora de l'UKF. Les diferents hipòtesis i aproximacions que s'han considerat en la definició dels coeficients d'aquest polinomi porten un error associat que s'ha demostrat que és, com a mínim, comparable amb l'error de l'UKF. Tot i així, la incorporació implícita de termes de segon ordre en els residuals resulta en una millora significativa de les prestacions del filtre.

Alguns dels resultats numèrics d'aquesta nova formulació també s'inclouen en aquest treball utilitzant el mateix exemple i configuració de referència utilitzats en [36] que posa de relleu, de manera simplificada, les dificultats que es troben en la combinació d'observacions per al vol de satèl·lits en formació.

4.3 Extensió de la Llei de Control de Cucker i Smale al Vol Espacial de Formacions

En aquesta secció es resumeix el contingut del treball [35], que ha estat publicat a la revista Journal of Guidance, Control, and Dynamics l'any 2009.

El comportament emergent que mostren molts grups d'animals ha atret recentment l'atenció de grups de recerca en enginyeria espacial (e.g., [41]) com a font d'algorismes prometedors per al control de formacions. En aquest article, estenem un model de comportament, inicialment dissenyat per Cucker i Smale a [8], a formacions de vol espacial per a l'adquisició i manteniment relaxat de les formacions.

El model de CS s'inspirava en el comportament emergent que mostraven grups biològics de partícules que, amb velocitat constant, modificaven la seva direcció amb la mitja de les direccions de les partícules veïnes [48]. Els autors de [8], en canvi, proposaven un model d'interaccions on cada individu modifica la seva velocitat amb la mitja ponderada de les velocitats relatives respecte a la resta d'individus de la població. En aquest cas, els pesos depenen de la distància relativa entre dos individus tenint en compte, així, la major incertesa associada al coneixement de la posició i velocitats relatives d'individus llunyans.

En aquell treball, els autors ofereixen una definició de pesos per a la ponderació de les velocitats relatives per a la que caracteritzen les condicions necessàries per al sorgiment d'un comportament collectiu. En aquest cas, els autors demostren que, sota certes condicions, el grup acabarà movent-se com un sòlid rígid amb velocitat constant i que no s'acabarà partint en grups menors d'individus.

En [35], estenem aquest model al camp espacial modificant la velocitat d'un satèl·lit amb l'acceleració relativa respecte el geocentre de la formació i la mitja ponderada de les velocitats relatives d'acord al model de CS. Basant-nos en els resultats de Cucker i

4. RESUM EN CATALÀ

Smale, podem oferir directament una caracterització dels paràmetres involucrats en el control que garanteix que el grup inicial tendirà a moure's com un sòlid rígid amb la dinàmica definida per al centre geomètric de la formació de satèl·lits.

En l'article incloem una extensa discussió sobre la possibilitat de càlcul en paral·lel i les necessitats de comunicació entre vehicles associades a aquest algorisme. També es preveuen i discuteixen les possibles limitacions del sistema de control, com ara la discretització de les accions de control i capacitats màximes i mínimes dels motors.

Per tal d'avaluar les prestacions d'aquest algorisme de control, hem considerat la missió Darwin com a escenari de referència. En particular, les prestacions del control de CS son avaluades al llarg de l'òrbita de transferència entre una òrbita terrestre i una òrbita halo al voltant del punt de libració L2 del sistema Terra-Sol. Una de les opcions de desplegament que es van considerar per a Darwin consistia en enviar els satèl·lits separadament a l'òrbita halo mantenint una formació relaxada.

Per tal d'avaluar detalladament les característiques d'aquest nova llei de control hem realitzat un anàlisis de sensibilitat extensiu utilitzant simulacions numèriques. Concretament, hem identificat els diferents paràmetres inicials i de configuració involucrats tant en el control com en la definició de l'escenari i, per a cadascun d'aquests paràmetres, hem considerat diversos valors i realitzat les simulacions corresponents. Els resultats d'aquestes simulacions s'han avaluat basant-nos en dos indicadors: la separació màxima respecte la trajectòria de referència i el cost energètic o Delta v total.

Per tal de poder comparar aquests resultats, hem pres com a referència els resultats presentats a [17]. En aquest treball, els autors presenten una nova estratègia basada en l'existència de certs cons al voltant de l'òrbita de transferència amb els seus centres sobre l'òrbita i amb la característica especial de que l'acceleració radial relativa sobre les generatrius dels cons és zero. Aquesta estratègia, anomenada com a control ZRRAC, també es va avaluar sota el mateix escenari de l'òrbita de transferència de Darwin utilitzant simulacions numèriques i amb l'objectiu de mantindre una formació relaxada.

Les simulacions numèriques han mostrat la importància del calibratge dels paràmetres de configuració de l'algorisme de control CS. Així, la configuració òptima dels paràmetres s'ha de basar en les característiques específiques de cada missió, principalment, el rang de possibles velocitats relatives inicials, i els temps màxims entre maniobres consecutives. Sota configuracions òptimes, l'algorisme de CS ofereix variacions mínimes de les distàncies relatives respecte els valors inicials al mateix temps que minimitza el cost

energètic. L'algorisme s'ha validat incloent soroll en les dades de navegació (posició i velocitat) i ha demostrat una sòlida robustesa. Finalment, la comparació entre els algorismes CS i ZRRAC, quan aquesta han estat possible, ha mostrat que el primer redueix significativament el cost energètic mentre ofereix resultats similars o fins i tot millors en termes de la separació entre vehicles.

En conclusió, l'algorisme CS ha mostrat ser un candidat apropiat per a l'adquisició i manteniment relaxat de formacions al llarg d'aquesta òrbita de transferència. Tot i així, l'àrea d'aplicació d'aquesta estratègia no es limita aquest tipus d'òrbita, sinó que també es pot considerar a l'espai profund, on les pertorbacions de la dinàmica son mínimes. La idoneïtat d'aquesta estratègia en entorns planetaris POE pot ser un tema d'investigació futura, amb especial atenció a la comparació de prestacions respecte l'altitud de la formació.

4.4 Dinàmica Relativa i Control per al Vol en Formació d'un Telescopi Virtual de Dos Elements en Òrbita Molt El·líptica

Aquesta secció resumeix el contingut de l'article [33], que va ser presentat al 21st International Symposium on Space Flight Dynamics l'any 2009, i publicat a les actes corresponents.

El l'article [35], hem presentat un algorisme per a l'adquisició i manteniment relaxat d'una formació basat en un model de comportament en grup. Aquest control, però, pot no ser apropiat per a l'adquisició d'una formació geomètrica específica ja que el control CS no garanteix una configuració final concreta. Un cop els satèl·lits estan en formació, el control CS pot ser usat per a mantindre la formació com un sòlid rígid. Per tal de seguir una trajectòria de referència específica s'ha d'escollir un sistema de referència apropiat, tal que les posicions relatives en aquest sistema siguin constants al llarg de la trajectòria de referència. Això pot donar lloc a utilitzar sistemes de referència força complicats i poc intuïtius. A més, els errors de modelat de la dinàmica relativa i les limitacions en el hardware poden portar a una ràpida violació dels exigents requisits de

la formació. Tot això pot fer que l'estratègia de CS no sigui apropiada per a mantindre una formació amb gran precisió.

Aquest és el cas, per exemple, d'un telescopi virtual que ha d'estar perfectament alineat amb el cos observat. L'objectiu principal de [33] és el disseny i validació d'un algorisme de control per a una plataforma virtual que no segueix una trajectòria relativa natural, com és el cas de la missió PROBA-3 [49]. Aquesta és una missió tecnològica que té com a objectiu principal provar algunes de les noves millores tecnològiques per a la navegació i control autònoms per al vol en formació. Com a principal càrrega científica, la formació portarà un ocultador i un coronògraf per observar la corona solar. Amb aquest objectiu, els dos satèl·lits que constitueixen aquesta missió han d'estar perfectament alineats amb el Sol.

La dinàmica relativa entre el coronògraf i la seva trajectòria de referència depèn directament de la posició del Sol i l'ocultador. En aquest article, primer analitzem la dinàmica relativa d'una formació de dos satèl·lits a una distància base de 150 m al llarg d'una Òrbita Molt El·líptica (HEO), tal i com està previst per a PROBA-3. Amb aquest objectiu, quantifiquem la magnitud de les acceleracions relatives degudes a les principals forces, e.g., la gravetat terrestre, variacions del potencial gravitatori, i la Pressió de Radiació Solar (SRP). Degut a les diferents condicions d'il·luminació dels dos satèl·lits, ja que un projecta la seva ombra sobre l'altre, les dues forces principals que defineixen la dinàmica relativa son la gravetat terrestre i la SRP. Per tal de tindre en compte l'ombra que projecta l'ocultador sobre el coronògraf, proposem un model per a aquesta ombra i el càlcul del diferencial de SRP.

Basat en l'anàlisis de la dinàmica relativa, proposem tres lleis de control per a l'adquisició i manteniment de la formació tal i com es deriven d'aproximacions diferents de la dinàmica relativa. La primera llei de control consisteix en dos termes: l'acceleració relativa per a cancel·lar la variació de la dinàmica respecte la seva referència i un terme lineal per a aconseguir la formació. L'acceleració relativa l'aproximem per les dues forces principals, és a dir, la gravetat terrestre i la SRP, mentre que el terme lineal es defineix per una matriu Hurwitz -amb pols sobre el semiplà esquerra del pla complex-. Ja que aquesta aproximació de la dinàmica relativa no és lineal, aquest control s'ha anomenat com control no lineal en contrast amb els altres dos.

Aquests altres dos controls es basen en aproximacions lineals de la dinàmica relativa. Sota aquesta hipòtesis, dissenyem una matriu de guany per tal de garantir que la

trajectòria real tendeixi a la de referència. Amb aquest objectiu, primer considerem les aproximacions necessàries per a la linealització de la dinàmica. Com a resultat, el terme de la SRP s'ommet completament en aquesta aproximació, igual que la component constant de l'acceleració relativa deguda a la gravetat terrestre. Aquesta aproximació és, llavors, utilitzada per a definir dos controls lineals en el vector d'errors.

El control de posicionament de pols robust considera l'algorisme de KNV per a calcular la matriu de guany, mentre que el control LQR, a més a més, considera una funció potencial de cost i dissenya la matriu de guany per tal de minimitzar el valor d'aquest potencial. Aquests algorismes tenen associats uns paràmetres de configuració -la definició dels pols i les matrius de pes dels errors i magnitud del control, respectivament- que s'han calibrar per a cada problema.

Els tres controls s'han comparat utilitzant simulacions numèriques. Per fer-ho, hem agafat com a referència la missió espacial de la ESA PROBA-3 com a escenari de referència. Més concretament, hem considerat la fase experimental on els satèl·lits han d'adquirir la formació per prendre observacions de la corona solar i s'ha de mantindre amb gran precisió durant el pas per l'apogeu. En les simulacions s'han considerat les dues òrbites HEO que eren candidates a l'òrbita de referència quan aquest estudi va arrancar [49]. Aquestes dues òrbites tenen períodes 1 i 3 dies, respectivament, sent la primera la seleccionada finalment per a PROBA-3 [40]. Les característiques específiques de l'òrbita, fase experimental, i modes d'operació també s'han introduït en l'article juntament amb altra informació rellevant per a la definició de l'escenari.

L'article descriu completament la plataforma experimental desenvolupada per a la validació i comparació de les lleis de control, incloent els models de la dinàmica, el sistema de metrologia per a la navegació relativa i les característiques completes dels models de Guiat, Navegació i Control (GNC) rellevants a aquest estudi.

La importància del calibratge per a cadascun dels algorismes queda manifesta en la primera part dels resultats. Tal i com s'explica en la secció "Results and Discussion", valors no apropiats poden resultar en la saturació dels motors, convergència lenta, o oscil·lacions d'alta freqüència dels errors de posicionament. Com a exemple, es mostren els resultats per al control nolineal. Finalment, es discuteix el paper dels paràmetres de configuració durant el calibratge i es compara el procés entre ells, sent el control LQR el de calibratge més senzill i intuïtiu.

Sota configuracions optimitzades, però, tots els controls ofereixen resultats similars i poden reduir l'error inicial en posició respecte la trajectòria de referència d'uns quants metres al nivell del centímetre, d'acord a les simulacions que es presenten. La principal diferència consisteix en la reducció de l'error quan els models de la dinàmica relativa inclosos en el control són més acurats, tal i com és el cas del control no lineal. Tot i així, la inclusió de termes no lineals en la dinàmica relativa només millora els resultats un cop els satèl·lits ja estan en formació i les acceleracions relatives son prou grans, en comparació amb la magnitud del control, és a dir, a poca altitud. Altrament, el terme lineal en l'error de control inclòs en el càlcul del control absorbeix els errors de modelat i fa que tots els controls ofereixin resultats similars.

4.5 Control Relatiu d'un Telescopi Virtual en Òrbita Molt El·líptica usant GNSS i Metrologia Òptica

Aquesta secció resumeix el contingut de l'article [32], que ha estat enviat per a avaluació i corresponent publicació, si s'escau, a la revista Journal of Guidance, Control and Dynamics el gener del 2010, com a nota d'enginyeria.

En aquest article, continuem el treball anterior i desenvolupem estratègies de control per a l'adquisició i manteniment precís d'un telescopi virtual que ha d'estar perfectament alineat amb el cos observat i seguir, així, una trajectòria no natural. De nou, la missió PROBA-3 ha estat presa com a referència. Motivats per les bones prestacions del control LQR, la seva simplicitat d'implementació, i el reduït cost computacional abord, tornem a considerar-lo per a l'adquisició de la formació. Per tal de reduir possibles contribucions constants a l'error després d'estabilitzar-se la solució, considerem també una extensió de l'LQR que inclou un terme integral de l'error a partir de l'estabilització. Aquest nou control l'hem anomenat com a LQRI i té com a objectiu el manteniment precís de la formació.

Aquests dos algorismes s'han implementat en una plataforma de vol en formació per a la seva validació sota un entorn realista. La plataforma de vol en formació (FFTB) del centre d'operacions de l'agència alemanya GSOC té com a objectiu la validació i anàlisi d'algorismes de GNC. Aquesta plataforma emula la dinàmica dels satèl·lits,

inclou els algorismes de GNC, un simulador de la senyal GPS Spirent GS7700 i dos receptor Phoenix GPS de freqüència simple.

Per a la validació d'aquest esquema de control, hem considerat els algorismes de navegació previstos per a la missió PRISMA. Aquesta missió, també tecnològica, té com a objectiu la validació de tecnologia de sensors i motors i demostrar capacitat d'autonomia en el vol en formació i consisteix en dos satèl·lits volant en formació en òrbita heliosíncrona. Els algorismes de navegació per a PRISMA processen observacions GPS per a la navegació relativa, tal i com està previst per a la navegació PROBA-3 a altituds baixes i s'ha reutilitzat en les simulacions actuals. Degut a les diferències substancials entre PRISMA i PROBA-3, alguns canvis han estat necessaris a la plataforma, tal i com es descriuen en l'article.

A partir d'aquestes simulacions hem analitzat les prestacions del sistema complet de GNC en detall durant un període orbital, amb l'excepció d'un petit interval corresponent al pas sobre el perigeu. Primer, hem analitzat les prestacions de la navegació relativa utilitzant GPS i, després, utilitzant un sistema òptic de metrologia per a altituds superiors. Després hem caracteritzat el sistema de guiat i, finalment, estudiem les prestacions dels algorismes de control per als modes d'adquisició i manteniment precís. Com a resultat global, la interacció del sistema complet de GNC permet una reducció de l'error de posició respecte la seva referència d'uns 8 m al nivell del centímetre.

Finalment, suggerim la possibilitat de millorar la precisió de les estimacions de la velocitat relativa quan utilitzem observacions òptiques per tal de reduir les oscil·lacions del control i, com a resultat, reduir el cost associat a aquesta estratègia. Segurament, això es podria aconseguir millorant el filtre d'estimació implementat, en primera aproximació, per al sistema de navegació òptic.

En resum, hem desenvolupat un algorisme de control simple i hem provat la seva validesa per acomplir exigents requisits de control. Les simulacions de l'escenari de PROBA-3 s'han d'interpretar com un exemple realista, tot i que l'aplicació d'aquesta tècnica no es limiti a aquesta missió sinó que es pot estendre fàcilment a altres missions.

Appendix A

Appended Papers

In this appendix, we include a copy of the five papers that form the core of this graduate research work. They are sorted chronologically to better expose how research ideas and algorithms evolved over time. Two of the papers are published as conference proceedings, two as journal papers and, the last one, submitted for publication in a journal paper. All five are peer reviewed.

- L. Perea, J. How, L. Breger, and P. Elosegui. Nonlinearities in sensor fusion. Divergence issues in EKF, modified truncated SOF, and UKF. In AIAA, editor, *Proceedings of the AIAA Guidance Navigation and Control Conference and Exhibit*, pages 1–16, Aug. 2007. Paper No. AIAA-2007-6514.

  Cited in [14, 19, 20, 34].

- L. Perea and P. Elosegui. New State Update Equation for the Unscented Kalman Filter. *Journal of Guidance, Control, and Dynamics*, 31(5):1500–1504, Sept. 2008.

  Cited in [11].

- L. Perea, G. Gómez, and P. Elosegui. Extension of the Cucker–Smale Control Law to Space Flight Formations. *Journal of Guidance, Control, and Dynamics*, 32(2):527–537, 2009.

  Cited in [4, 5, 6, 7].

- L. Perea, S. D'Amico, and P. Elosegui. Relative Formation Flying Dynamics and Control of a Two-Element Virtual Telescope on a HEO. In CNES,

editor, *Proceedings of the 21st International Symposium on Space Flight Dynamics (ISSFD)*, pages 1–15, Sept. 2009.

- L. Perea, J.-S. Ardaens, S. D'Amico, and P. Elosegui. Relative Control of a Virtual Telescope in a High Elliptical Orbit using GNSS and Optical Metrology. *Journal of Guidance, Control, and Dynamics*, 2010 (submitted).

Nonlinearity in Sensor Fusion: Divergence Issues in EKF, modified truncated SOF, and UKF

L. Perea*   J. How†   L. Breger†   P. Elosegui*

   Relative navigation is a challenging technological component of many planned NASA and ESA missions. It typically uses recursive filters to fuse measurements (e.g., range and angle) from sensors with contrasting accuracies to estimate the vehicle state vectors in real time. The tendency of Extended Kalman filter to diverge under these conditions is well documented in the literature. As such, we have investigated the application of the modified truncated Second-Order Filter (mtSOF) and the Unscented Kalman filter (UKF) to those mission scenarios using numerical simulations of a representative experimental configuration: estimation of a static position in space using distance and angle measurements. These simulation results showed that the mtSOF and UKF may also converge to an incorrect state estimate. A detailed study establishes the divergence process of the mtSOF and UKF, and designs new strategies that improve the accuracy of these filters.

I.   Introduction

Formation flying is expected to become a core technology component of future space missions such as Symbol-X, TPF, and DARWIN. Missions demonstrating formation flying technologies, e.g. the Proba 3 concept[1] of the European Space Agency (ESA), are under consideration at space agencies worldwide. These missions may combine measurements from various sensors,[2] likely with different accuracies, to meet position and attitude requirements defined both for the individual satellites and for the formation. Measurements such as range and bearing will require nonlinear estimators that are robust and can also operate autonomously for extended periods of time.[3] This study investigates divergence properties of high-order filters, in particular the unscented Kalman filter (UKF), in the presence of nonlinearities; and evaluates proposed modifications to improve filter performance.

The extended Kalman filter (EKF) is a nonlinear filter that is used extensively because it usually provides very good estimation performance and has a straightforward implementation. However, the EKF has been shown to fail (i.e., to diverge or to converge to an incorrect solution) in many object tracking applications where the dynamic models, measurement models, or both, are not linear functions of the state vector.[4,5] An example of this is determining the orbit of a satellite formation using Global Positioning System (GPS) measurements and inter-vehicle ranging (e.g., using microwave signals), for which EKF has been shown to be unreliable.[6] Huxel et al. characterized the error associated with the EKF and the modified Gaussian second-order filter due to the combination of inertial and relative range measurements with different accuracies. Plinval[7] and Mandic[8] further analyzed the divergence process of the EKF under similar conditions, and investigated the performance of an alternative recursive filter focusing on an *ad hoc* increase of the measurement noise levels,[7–10] a technique also known as "Bump-up."

There are several other filters in the literature that have been designed to deal with nonlinear measurements,[5–7, 11–18] with respect to the state vector. These filters use different approximations of the measurement models, different approximations of the probability density functions, or both. For example, there exists a large set of filters that are variations of the EKF. The iterated EKF (IEKF) is known for its accuracy with nonlinear measurement models conditioned to ensure that the system is fully observable.[14] Its main drawback is the computational load associated with the additional filter iterations that are required. The linear regression Kalman filters (LRKF) represent another set of variants that approximate the state/measurement estimate and the associated uncertainty by a statistical linear regression through a well chosen set of "sigma

*Institute for Space Sciences, CSIC–IEEC, Barcelona, Spain
†Department of Aeronautics and Astronautics, MIT, Cambridge, MA, USA

points". This process allows multiple moments of the probability density function and terms of the Taylor-series expansion of the dynamic/measurement models to be considered. Some examples of this family are the central difference filter, the first-order divided difference filter, and the recent unscented Kalman filter (UKF).[13, 14, 19] These filters require the evaluation of the measurement model at several points, but, in contrast with the EKF and IEKF, they avoid the computation of the Jacobian of the models. This makes them particularly well suited to the case where the evaluation of the Jacobian is complex or computationally expensive.

Another important set of filters are the high-order filters. The second-order filters (SOF) are probably the best known among them. These filters approximate the models by a high-order Taylor approximation, and assume that the third and higher-order moments of the probability functions are a function of the covariance.[15] The complexity and computational load required for the implementation of these types of filters typically make their implementation unfeasible, particularly in the vector case ($x \in \mathbb{R}^n$, $n > 1$).[15] In the case of the SOF family, some simplifications have been designed to avoid the complexity of implementing a full SOF. For example, the mtSOF, which accounts for bias correction terms due to nonlinearities in the models,[15] is commonly used.

Particle filters approximate the full probability distribution, not only the mean and the variance, by using a finite set of samples. These filters use the sequential sampling and resampling according to an "importance function" to provide much better performance than Kalman filters. The improved performance is especially pronounced when using nonlinear models (e.g., object tracking using bearing sensors[5]), or non-Gaussian distributions. However, the high computational cost associated with using the large number of samples required makes them unsuitable for almost real-time navigation applications.[5, 12]

This study is aimed at characterizing the error due to nonlinear measurements (with respect to the state vector) using different kinds of filters suitable for near real-time missions, such as those presented above. For this purpose, we evaluated the estimation performance of a representative set of filters: the EKF,[4, 9, 15] bump-up strategies based on the EKF,[6–10] the mtSOF,[15] and the UKF.[5, 13] We used a popular experimental case[5, 7, 8] that allows full isolation of the performance of the update equations from the propagation equations. We evaluated the estimation performance and long-time stability of these filters under identical experimental conditions, and designed possible modifications to improve their performance, when possible.

In the following sections, we introduce previous filters using a unified approach for describing both prediction and update phases. This notation permits straightforward comparisons between filters and makes clear the respective roles of each term in the filter equations. Because of their common structure we will refer to this kind of filters as Kalman-type filters in the sequel. The errors and divergence processes of these Kalman-type filters are characterized in detail. Then, proposed modifications to these filters are described that improve their performance in the presence of nonlinear measurement models. These modifications have been evaluated for a large set of experimental configurations.

II.   Description of Kalman-type filters

The extended Kalman filter, the *modified truncated* second-order filter, and the unscented Kalman filter all belong to a common family of Kalman-type filters. They are used to estimate the n-dimensional state $x \in \mathbb{R}^n$ of a process that is governed by an *almost-linear* stochastic differential equation,

$$\dot{x} = f(t, x)dt + G(t, x)d\beta(t)$$

through the measurements $z \in \mathbb{R}^m$

$$z = h(x) + v$$

where $\dot{x}$ is the time derivative of the state vector x, n is the dimension of x, f is the dynamic model function, t is time, G is an n-by-s function, β is an s-vector dimensional Brownian motion of diffusion $Q(t)$, z is the measurement vector, m is the dimension of z, h is the measurement modeling function, and v is the measurement noise ($\sim N(0, R)$). The state estimation procedure has two distinct phases: first, it predicts the statistics that describe the distribution of the state x at time $t - \Delta t$ to time t, when new measurements will be available; and second, it updates the predicted state estimate as new measurements become available.

Kalman-type filters are based on the assumption that the state, measurement, and error distributions can be characterized by only two statistics: the mean and the covariance. Higher order central moments are assumed small enough to be neglected. Therefore, the equations used to propagate and update the state

estimates are based on different approximations of the following conditional expectations

$$\hat{x}_k^- = E[x(t_k)|z(t_{k-1}) = z_{k-1}] \tag{1}$$

$$P_{xx,k}^- = E[(x(t_k) - \hat{x}_k^-)(x(t_k) - \hat{x}_k^-)^T|z(t_{k-1}) = z_{k-1}] \tag{2}$$

$$\hat{x}_k^+ = E[x(t_k)|z(t_k) = z_k] \tag{3}$$

$$P_{xx,k}^+ = E[(x(t_k) - \hat{x}_k^+)(x(t_k) - \hat{x}_k^+)^T|z(t_k) = z_k] \tag{4}$$

where the character $^\wedge$ denotes estimated value, k is a time index, $^-$ indicates a predicted value, $z(t)$ is the measurement variable, z_k is the measurement, $P_{xx,k}$ is the covariance matrix of the state estimate, ^{T} denotes matrix transpose, and $^+$ indicates an updated term.

The approximations of the conditional expectations (1) and (2) corresponding to the prediction phase are called prediction equations, and they vary between filters. The EKF propagates the state estimate statistics (i.e., the mean and the covariance) by integrating the linearized differential equations. Therefore, the statistics estimated using the EKF are linear approximations of the true mean and true covariance matrix. On the other hand, the mtSOF and UKF may propagate the state statistics using higher-order terms of the nonlinear dynamic model f, thus increasing their accuracy with respect to the EKF. In particular, the mtSOF includes second-order terms of the dynamic model by using the first and second derivatives of f, thereby increasing the complexity of the algorithm implementation in many problems.[15] The UKF circumvents such increased complexity by generating a set of well distributed points around the current estimate, propagating this set of sigma points to the next epoch, and then re-computing the statistics from the resulting set of sigma points. Depending on the number and distribution of the original sigma points, the UKF can include high-order terms of the dynamic model f with adjustable accuracy for these equations, though this can also add complexity in the selection of the sigma points.[12]

To approximate the conditional expectations (3) and (4) of the update phase, all previous filters use the following approximations, which are usually referred to as update equations:

$$K_k = P_{xz,k}P_{zz,k}^{-1} \tag{5}$$

$$\hat{x}_k^+ = \hat{x}_k^- + K_k(z_k - \hat{z}_k) \tag{6}$$

$$P_{xx,k}^+ = P_{xx,k}^- - P_{xz,k}(P_{zz,k})^{-1}P_{xz,k}^T \tag{7}$$

where K_k is the Kalman gain matrix, P_{xz} is the covariance matrix between the state and the measurement, P_{zz} is the covariance matrix of the measurements, z is a vector of measurements, $\hat{z}$ are the expected measurements, and $(z_k - \hat{z}_k)$ are the innovations or measurement residuals.

Equations (5) - (7) correspond to a linear function of the measurement residuals, and that the coefficients are functions of $\hat{x}_k^-$, P_k^-, and h. When h is a nonlinear function, the coefficients are also nonlinear functions of the state space statistics and each filter generally computes them with the same degree of accuracy as that used in the propagation equations. For the computation of $\hat{z}_k$, P_{zz}, and P_{xz}, the state statistics $\hat{x}_k^-$ and P_k^- are transformed to the measurement space using the same approximations of (1) and (2). The EKF transforms mean and covariance using a linearization of the measurement function h; the mtSOF transforms these statistics using the first and second derivatives of h; the UKF generates a set of sigma points for this transformation.

Figure 1 shows the performance of these filters for the case of a static vehicle (i.e., $f(t,x) = 0$) in $\mathbb{R}^2$ without process noise ($Q(t) = 0$), using linear measurements (e.g., $h(x) = x$), and independent measurement noise levels (R is diagonal, with elements $\sigma_1 = 2.5\text{E}{-}5$ and $\sigma_2 = 6\text{E}{-}3$ in the example shown). Under this configuration, both the EKF and the mtSOF coincide because there are no second-order terms, and all three filters provide good estimates from the first iteration, as expected for linear measurements. The following sections analyze the suitability of the linear assumptions of the update equations in the EKF, mtSOF, and UKF in experimental configurations that involve highly nonlinear measurements.

III.   Description of the experimental configuration

In order to address the accuracy of the update equations, we will consider the estimation of a fixed position in Cartesian coordinates $x = (x_1, x_2)$ in $\mathbb{R}^2$ (i.e., a system with no dynamics $\dot{x} = f(t,x) = 0$ and $Q \equiv 0$ as in Figure 1), thus effectively isolating the prediction phase from the update phase. The nonlinear measurements considered are distance $r = \sqrt{x_1^2 + x_2^2}$ and angle $\theta = \arctan(x_2/x_1)$. This configuration
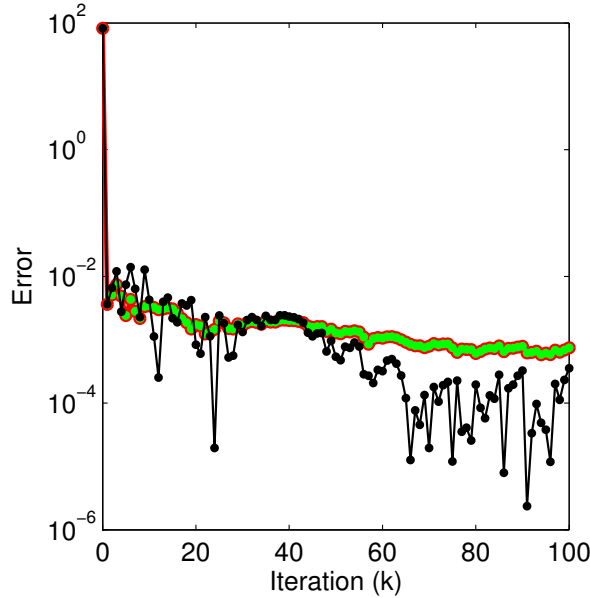
Figure 1. Variation of the (red) EKF, (green) mtSOF, and (black) UKF position error of a static vehicle using linear measurements. Note that the vertical axis is in logarithmic scale.

was previously employed by several authors[5,7,8] to evaluate the performance of the EKF. It is particularly well-suited for filter evaluation because of its simplicity and nonlinearity.

The propagation equations associated with this problem are identical for all filters:

$$\hat{x}_k^- = \hat{x}_{k-1}^+ \tag{8}$$

$$P_{xx,k}^- = P_{xx,k-1}^+ \tag{9}$$

We have chosen to make the distance measurements significantly more accurate than the angle measurements to be representative of sensor suites on possible future proposed formation flying missions.[7,8,20] As a baseline configuration $\tilde{x}_{true} = (100, 100)$ units; the covariance matrix of measurement noise R is a diagonal matrix with a radial measurement noise level σ_r^2 of 2.5E−5 square units, and an angular noise level σ_θ^2 of 6E−3 square radians; an a priori state estimate $\hat{x}_0 = (20, 80)$; and the a priori state uncertainty $P_{xx,0} = \sigma^2 I$, where $\sigma = 100$. Other values will be used in the sensitivity analysis (see below). Perfect measurements have been used as realizations of the measurement variable z, i.e., $z(t_k) = h(\tilde{x}_{true})$ for every k. This represents a best-case scenario in which measurements are better-than-expected under normal experimental conditions.

IV.   Divergence process of the EKF

To introduce the problem of filter divergence, an analysis of the EKF divergence process is presented first. The explicit expressions for the coefficients of the update equations (6)–(7) in the EKF are:

$$\hat{z}_k = h(\hat{x}_k^-) \tag{10}$$

$$P_{zz,k} = R + H_k P_{xx,k}^- H_k^T \tag{11}$$

$$P_{xz,k} = P_{xx,k}^- H_k^T \tag{12}$$

where $H_k = \frac{\partial h}{\partial x}\big|_{\hat{x}_k^-}$ is the Jacobian matrix of $h(x)$ evaluated at $x = \hat{x}_k^-$.

The EKF linearizes the nonlinear measurement function h around the current predicted state estimate and ignores higher-order terms. Although widely used, the EKF is thus only reliable for systems that are almost linear within the time scale of the update interval.[19] Plinval[7] and Mandic[8] evaluated the performance

of this filter for the problem described in Section III and found that it failed to converge to the true position regardless of the number of filter iterations, a process that they diagnosed as filter divergence. They determined that the divergence was due to an over-reduction of the state covariance matrix in all dimensions, which, in turn, was caused by the nonlinearities of the measurement model. They found that the true state vector lies outside the ellipsoid that approximates the confidence area of the estimated state vector after a few filter iterations. This section builds on that example to further investigate the problem of filter divergence.

Figure 2(a) shows the experimental configuration after the first filter iteration. The estimation process starts with the initial state estimate at the (unitless) position $\hat{x}_0^+ = (20, 80)$, and the true position $\tilde{x}_{true} = (100, 100)$. During the first measurement update, the radial component of the measurement residual is projected into the direction of $\hat{x}_1^- = \hat{x}_0$ from the origin of coordinates -this direction will be referred to as radial direction in the sequel-, and the angular component of the measurement residual is projected onto its tangential direction due to the linearization process of the measurement model. Due to the linear model of the measurement update equations, both contributions are combined through simple addition, leading to the new state estimate $\hat{x}_1^+ = (77.36, 126.43)$. The resulting error in the update state estimate $\tilde{x}_{true} - \hat{x}_1^+$ is significantly large compared to the measurement noise R.
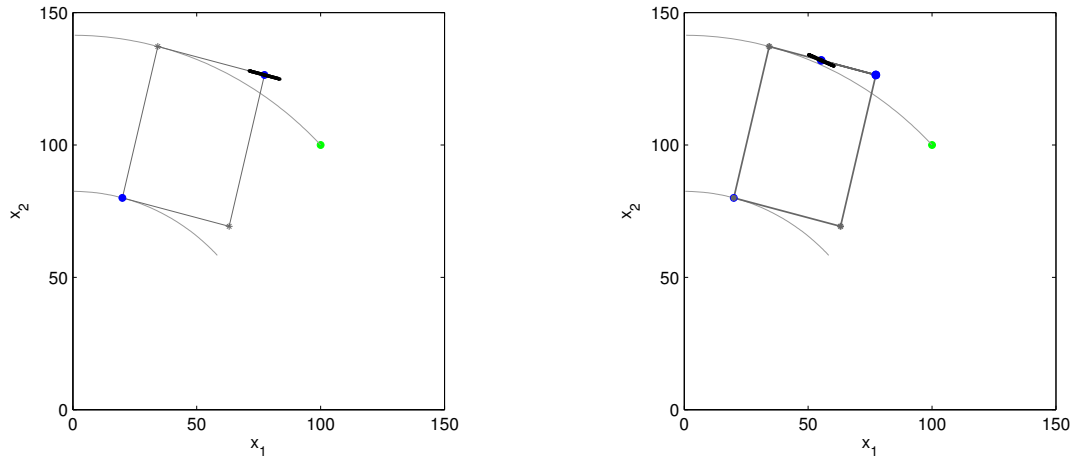
(a) First update process. This figure depicts (green) $\tilde{x}_{true} = (100, 100)$, (blue) $\hat{x}_1^- = \hat{x}_0 = (20 \quad 80)$, (grey) the new state variation due to the radial residual (along the radial direction), and to the angular residual (along the linearized angular direction), (blue) the resulting update state estimate $\hat{x}_1^+ = (77.36 \quad 126.43)$, and (black) the 1-$\sigma^2$ confidence area associated to the state covariance matrix $P_{xx,1}^+$. Note that the ellipse $P_{xx,1}^+$ has almost collapsed to an interval.

(b) Second update process. This figure depicts $\hat{x}_1^- = \hat{x}_0$, $x_2^- = x_1^+$, the new state variation due to the radial residual (along the linearized angular direction of $\hat{x}_0$ due to the erroneous correlation of $P_{zz,2}$), and to the angular residual (undetectable due to its small size), $\hat{x}_2^+ = (55.32 \quad 131.94)$. The resulting (black) 1-σ^2 confidence area associated to the state covariance matrix $P_{xx,2}^+$ has contracted so much that it can not be appreciated in this picture, for this reason we plotted 10^4-σ^2 confidence area.

Figure 2. EKF update process.

The state covariance update remains unaffected by the error in the state update because the former assumes a linear measurement model. The magnitude of the update state covariance is greatly reduced in all directions due to the small size of the measurement noise levels (R matrix). Due to the differences in the measurement noise levels, the confidence area has contracted faster in the direction of $\hat{x}_1^- = \hat{x}_0$ than in the linearized angular direction. The confidence area of the new state estimate corresponds to an ellipsoid with axis parallel to the eigenvectors of $P_{xx,1}^+$, that correspond to the radial and angular directions of $\hat{x}_1^- \neq x_1^+$. Figure 2(a) shows that the large reduction of the state covariance has allowed the solution $\tilde{x}_{true}$ to fall outside the 1-σ confidence area defined by $P_{xx,1}^+$.

After the first update, the radial and angular directions associated with the new state $\hat{x}_1^+$ have changed. Therefore, the eigenvectors of $P_{xx,1}^+$ do not correspond to the radial and angular directions of $\hat{x}_1^+$. This misalignment, together with the high condition number of the state covariance, result in a significant term appearing in the off-diagonal of $P_{zz,2} = (R + H_k P_{xx,2}^- H_k^T)^{-1}$. The presence of this term is interpreted by the

filter as indicating a correlation between the radial and the angular measurements, which leads the filter to a misinterpretation of the residuals during the next update. Figure 2(b) shows that the new measurement residuals are further misinterpreted leading to an update state estimate with a larger error than the first update. Since the covariance matrix update is independent of the residuals, the updated covariance matrix shrinks again in all directions ($P_{xx,1}^+$ has been magnified by 10^4 in Figure 2(b); see figure caption).

At this stage, the state covariance is sufficiently small compared to the measurement noise levels that the filter under-weights all new measurements. This is illustrated in Figure 3, which shows that the state estimate error remains effectively constant after two iterations. Henceforth, we refer as *apparent filter divergence*, or just filter divergence, to the situation in which a large error in the state estimate exists relative to a small state covariance matrix at steady state, which coincides with the definition used in references 4, 15.
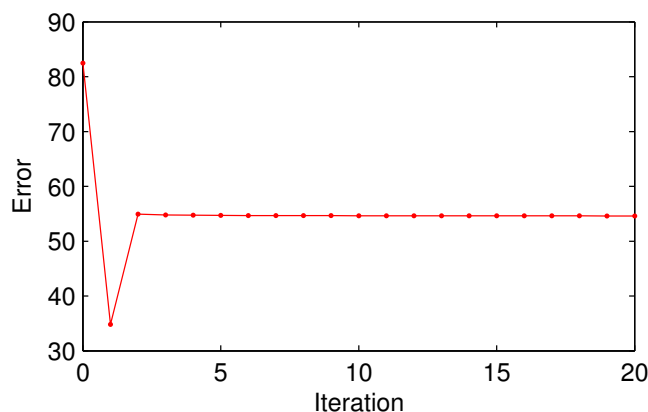
Figure 3. Variation of the EKF position error with filter iteration.

In summary, the example demonstrates that if the linear approximations of the measurement directions have a large dependence on the state estimate (i.e., $H(x) = \frac{\partial h(x)}{\partial x}$ is far from constant) and the measurements have very different noise levels, the linear update equations may lead the filter to diverge. To overcome the divergence of the EKF, both Plinval and Mandic investigated the possibility of artificially increasing the measurement noise levels to slow down the convergence process. This strategy will be referred to as bump-up EKF.

IV.A. Bump-up EKF strategies

A bump-up EKF strategy (B-EKF) tries to avoid the divergence of the filter by reducing the rate of convergence in the direction of the more accurate measurements, and "waits" for convergence in the less accurate directions. This strategy mitigates the over-reduction of the state covariance matrix. Additionally, the possible correlations in $P_{zz,k}$ due to a misinterpretation of the state covariance matrix will have a lower impact on the measurement update. The only difference in the formulae between these strategies and the EKF, is that a B-EKF will artificially increase the noise associated with the accurate measurements, and reduce this increment as a function of the confidence in current state vector estimates. Geometrically, this strategy means using larger and less eccentric confidence areas (or $P_{k,xx}^+$) compared to the EKF.

Based on this rationale, Plinval defined the following bump-up on the measurement noise level, which is assigned the label B-EKF 1:

$$\text{B-EKF 1:} \qquad R_{new} = R + H_k P_{xx,k}^- H_k^T \qquad (13)$$

The right-hand side term $R + H_k P_{xx,k}^- H_k^T$ corresponds to the linear approximation of the measurement estimate covariance $P_{zz,k}$ (i.e., equation (11)) and the new measurement covariance is then $P_{zz,k,new} = R + 2H_k P_{xx,k} H_k^T$. Hence, the artificial increase is expected to be reduced as the state estimate uncertainty decreases. At steady state, this strategy is nearly equivalent to the EKF.

Figure 4 shows the norm of the estimation error $||\tilde{x}_{true} - \hat{x}_k||$ as a function of filter iteration k for B-EKF 1, EKF, and other filters (see below). The remarkable improvement of the B-EKF 1 with respect to the

EKF is consistent with reference 7. Mandic generalized this bump-up strategy and defined:

$$R_{new} = R + \alpha H_k P_{xx,k}^- H_k^T \tag{14}$$

where $\alpha \in \mathbb{R}^+$. This author noted that the α value of the bump-up and the magnitude of the error at steady state were related. It is further stated that the α value that minimizes the error at steady state seemed to depend on the error of the a priori information, and that no method for selecting α a priori was known.[8]

Further building on these strategies, we designed several alternative bump-up strategies to increase the state or measurement error noise covariance matrices (P or R). The rationale behind these new B-EKF is twofold; first, to reduce the probability of over-reduction of the state covariance matrix by artificially increasing the measurement noise levels; and second, to create a measurement noise matrix with a confidence area in the state space that is circle-shaped, thereby partially canceling possible misinterpretations of the correlations in P. The following bump-up strategies are labeled B-EKF 2, 3, and 4,

$$\text{B-EKF 2:} \qquad R_{new} \quad = R + ||P_{xx,k}^-||H_k H_k^T \tag{15}$$

$$\text{B-EKF 3:} \qquad R_{new} \quad = ||J_k R J_k^T||H_k H_k^T \tag{16}$$

$$\text{B-EKF 4:} \qquad P_{xx,k,new}^- \quad = ||P_{xx,k}^-||I_n \tag{17}$$

where J is the Jacobian of $h^{-1}(r,\theta)$ assuming the existence of this inverse function.

Equation (15) has the same form as (13), and becomes identical when $P_{xx,k}^-$ is a multiple of the identity. The usage of $||P_{xx,k}^-|| \cdot I_n$, instead of $P_{xx,k}^-$, is equivalent to considering the minimum circular area that contains the 1-σ confidence area defined by $P_{xx,k}^-$. Therefore, an error in the direction of the eigenvectors would have a minor impact. Figure 4 shows that the performance of B-EKF 1 and B-EKF 2 are very similar.

The bump-up method in equation (16) considers equivalent noise levels for different types of measurements and bump-up for only the lower accuracy terms of the R matrix in order to create similar convergence velocities in all directions. In the numerical simulation considered, starting from a state estimate $\hat{x}_0 = (20, 80)$ units means that a radial error of 1 unit is equivalent to an error of 1 unit along the radial direction, while an angular error of 1 degree is equivalent to an error of ~ 1.4 units perpendicular to the radial direction. To compare the noise levels of different types of measurements, it is necessary to transform the measurement covariance matrix to the state space. Equation (16) uses a linear approximation, $J_k R J_k^T$, to apply such a transformation. In order to have comparable noises in the state space, this strategy uses $||J_k R J_k^T|| \cdot I_n$, and linearly transforms this covariance matrix back into the measurement space. The resulting R_{new} matrix, which is larger than R by construction, consists of comparable (in state space) noise levels for different types of measurements. Figure 4 shows that though the improvement relative to the EKF is significant, this bump-up performs worse than the previous B-EKF beyond the second iteration. Conceptually, the bump-up should affect all directions, not only the directions of the coarse measurements, thus effectively preventing over-reductions in any direction.

Equation (17) defines the only strategy that uses a bump-up of the state covariance $P_{xx,k}^-$ instead of the measurement covariance matrix R. It raises the lower accuracy terms of the state covariance matrix to impose a circularly shaped confidence area for the state estimate just before updating the state estimate with a new measurement. This minimizes the effect of a misinterpretation of the direction of the eigenvectors in the computation of $P_{zz,k}$, and $P_{xz,k}$. Figure 4 shows that this approach and the prior B-EKF provide similar performance for the current configuration. On a logarithmic scale, the improvement of the initial estimation using the bump-up strategies is approximately linear.

The main drawback of the B-EKF is that the speed of convergence, in terms of reducing the uncertainty associated to the state estimate, may decrease substantially with respect to the EKF.

V.   Divergence process of the mtSOF

As previously introduced, the second-order filter is probably the best known among the high-order filters. These filters approximate the models by a second-order Taylor series expansion,[15] but the complexity and computational load required for an implementation of the full-scale second-order filter typically makes its implementation unfeasible, particularly in the vector case ($x \in \mathbb{R}^n, \quad n > 1$).[15] In the case of the second-order filter family, some simplifications have been designed to avoid the complexity of the full-scale implementation while retaining many of its useful properties. The version presented hereafter is referred to as the modified
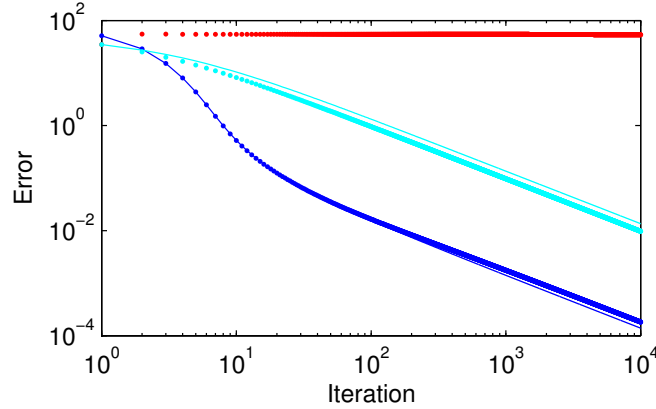
Figure 4. Variation of the position error for various bump-up strategies: (red) EKF, (blue dots) B-EKF 1, (blue line) B-EKF 2, (cyan line) B-EKF 3, and (cyan dots) B-EKF 4. Both axes are in logarithmic scale.

truncated second-order filter (mtSOF), which additionally assumes that the conditional density is nearly symmetric, and also that fourth and higher order even central moments can be neglected. The explicit update equations are:

$$\hat{z}_k = h(\hat{x}_k^-) + b_m \tag{18}$$

$$P_{zz,k} = R + H_k P_{xx,k}^- H_k^T - b_m b_m^T \tag{19}$$

$$P_{xz,k} = P_{xx,k}^- H_k^T \tag{20}$$

where $b_{m,i} = \frac{1}{2} tr\{\frac{\partial^2 h_i(\hat{x}_k^-)}{\partial x^2} P_{xx,k}^+\}$, and i denotes the index for the vector component of h. The expressions for $\hat{x}_k^+$, $P_{xx,k}^+$, and $P_{zz,k}$ are identical to equations (6), (7), and (12), respectively. Comparison of equations (10)–(11) and (18)–(19) shows that mtSOF is an EKF plus the b vector, which captures the second-order contribution of h.

Figure 5 shows the position error as a function of the filter iteration for the same experimental configuration presented in Section III. Comparison of Figures 5 and 3 shows that even though the mtSOF uses a second-order term b_m, any improvement over the EKF is marginal. Figure 5 also shows that mtSOF is very unstable. Inspection of the filter values reveals that the state covariance matrix does not retain its positive definite property after the first update. The $b_m b_m^T$ term causes a large reduction from $P_{xx,0}^+$ to $P_{zz,1}$ and, in turn, of $P_{xx,1}^+$. For this reason, the results of the filter in successive iterations become unrealistic and unpredictable. After a certain number of iterations, around 200, the filter reaches a steady state with an error of ~40 units and a state covariance matrix corresponding to an uncertainty smaller than 0.04 square units in the angular direction, and 2E−7 units in the radial direction. These results indicate that the filter diverges because the state covariance matrix experiences an over-reduction right at the first iteration for the experiment being considered.

V.A. Bump-up mtSOF

We investigated a bump-up strategy of the measurement noise level similar to those designed for the EKF. We implemented the bump-up strategy defined in equation (13), which we will refer to as B-mtSOF for consistency, because of the good performance obtained with the B-EKF 1 and the reduced computational load associated with the bump-up. Figure 5 shows the estimation error for the mtSOF and the B-mtSOF. In this example, the B-mtSOF avoids the tendency of the state covariance matrix to lose its positive definiteness for more than 20 iterations and, therefore, shows a significant improvement over the mtSOF. However, the updated state covariance matrix loses positive definiteness after iteration 23, making the filter performance unpredictable. This leads to a sudden state estimate degradation near iteration 100.
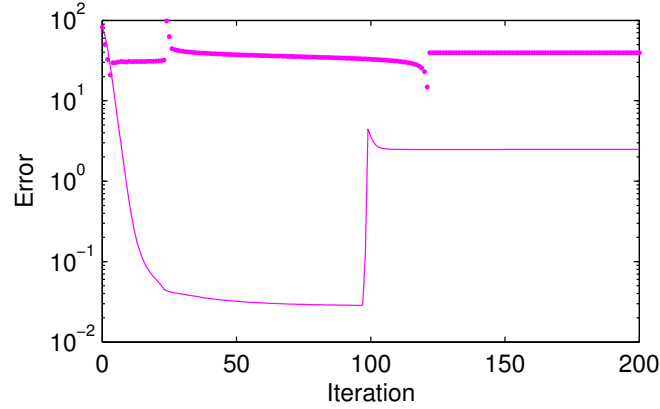
Figure 5. Variation of the state estimation error for the (dots) mtSOF and (continuous line) B-mtSOF.

VI. Divergence process of the UKF

The linear regression Kalman filters represent a set of EKF variants that approximate the state/measurement estimate and the associated uncertainty by a statistical linear regression through a well chosen set of points. This process allows multiple moments of the probability density function and terms of the Taylor approximation of the dynamic/measurement models to be considered. A representative example of this family is the UKF.[13, 14, 21] It requires the evaluation of the measurement model at several points, thereby avoiding the computation of the full Jacobian, in contrast with the EKF. This makes the UKF particularly well suited to the case where the evaluation of the Jacobian is complex or computationally expensive.

The explicit steps involved in updating the set of sigma points for this filter in absence of dynamics include the computation of:[5, 12, 22]

1. The sigma set from the predicted state and covariance matrix as

$$\mathcal{X}_k = \left[\begin{array}{ccc} \hat{x}_k^-, & \hat{x}_k^- + \gamma\sqrt{P_{xx,k}^-}, & \hat{x}_k^- - \gamma\sqrt{P_{xx,k}^-} \end{array} \right] \tag{21}$$

where the matrix $\sqrt{P_{xx,k}^-}$ is interpreted as a set of n column vectors, and γ is a constant.

2. The measurements associated with this sigma set

$$\mathcal{Z}_k = h(\mathcal{X}_k) \tag{22}$$

$$\hat{z}_k = \sum_{i=0}^{2n} W_i^{(m)} \mathcal{Z}_{i,k} \tag{23}$$

where $W_i^{(m)}$ and $W_i^{(c)}$ are a specific set of weights, m denotes mean, c denotes covariance, and i is the index of the sigma point (see reference [12] for additional details).

3. The expected correlations from the image set $\mathcal{Z}_k$ are

$$P_{zz,k} = R + \sum_{i=0}^{2n} W_i^{(c)} (\mathcal{Z}_{i,k} - \hat{z}_k)(\mathcal{Z}_{i,k} - \hat{z}_k)^T \tag{24}$$

$$P_{xz,k} = \sum_{i=0}^{2n} W_i^{(c)} (\mathcal{X}_{i,k} - \hat{x}_k^-)(\mathcal{Z}_{i,k} - \hat{z}_k^-)^T \tag{25}$$

$$\tag{26}$$

4. The update equations are the same as those used in the previous filters, i.e. equations (6)–(7).

American Institute of Aeronautics and Astronautics
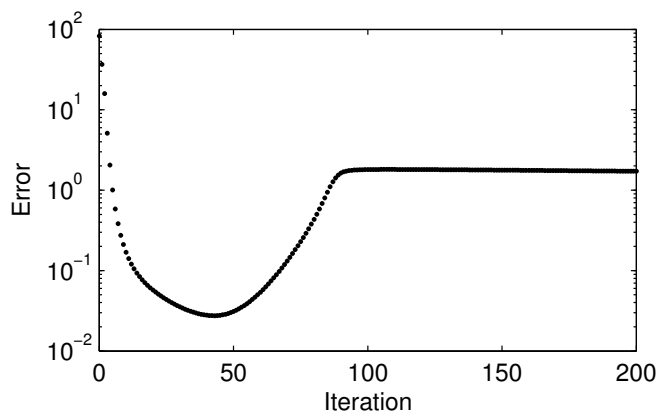
Figure 6. Variation of the state estimation error for the UKF.

Figure 6 shows the norm of the state estimation error as a function of filter iteration for the experimental configuration introduced in Section III. The error pattern of the estimated state of the UKF is counterintuitive because there is an initial phase of significant improvement (up to iteration ∼45), followed by a phase in which the error increases (between iterations ∼45–90), and a final phase where the improvement is marginal (beyond ∼90). Since the dynamic model of this example is static, the propagation equations cannot be the cause of this variation. To gain some insight into the relative accuracy of equations (10) and (23), Figure 7 shows the estimated measurement $\hat{z}_k$ after equations (10) and (23) for the UKF. This figure reveals that equation (23) is approximately four times more accurate than (10). This leads to an almost zero residual vector, and thus, a too small modification of the state estimate.
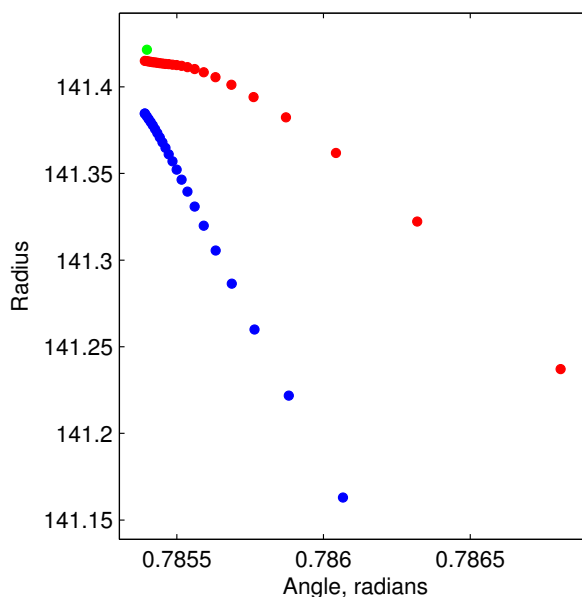
Figure 7. Measurement estimates $\hat{z}_k$ for the first 30 iterations using the (red) UKF equations and (blue) a linear approximation ($\hat{z}_k = h(\hat{x}_k^-)$). Within each curve, the time direction is from bottom-right to top-left. The true position $\tilde{z}_{true} = h(\tilde{x}_{true})$ is marked by a green dot.

The divergence process of the UKF can be summarized as follows:

1. At iteration number 14, the state estimate confidence area has contracted too much and the true

American Institute of Aeronautics and Astronautics

state $\tilde{x}_{true}$ falls outside the ellipsoid that approximates the confidence area $P_{xx,k}$ (see Figure 8(a) and 8(b)), as was the case when using the EKF with fewer iterates. Figure 8(c) shows the ellipsoid $P_{zz,k}$ that approximates the confidence area of the measurement estimate still includes the measurement corresponding to the true state $h(\tilde{x}_{true})$.

2. At iteration number 21, $h(\tilde{x}_{true})$ exits the ellipsoid defined by $P_{zz,k}$ (see Figure 8(d)).

3. Beginning at iteration number 29, the information from new measurements is misinterpreted by the filter and the state estimates begin moving away from the solution in the angular direction first, and then in the radial direction. The increasing condition number of $P_{xx,k}$ together with the discrepancy between the direction of the associated eigenvectors and the linear approximation of the measurements direction results in a significant correlation between radial and angular measurements in the P_{zz} matrix, as in the EKF example. This causes the residual information to be misinterpreted in the filter.
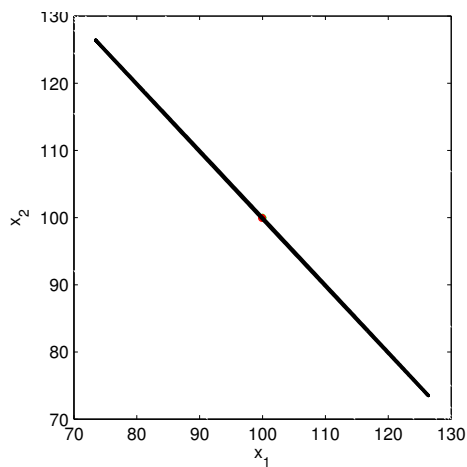
(a) (Black) 1-σ^2 confidence area for the (red) state estimate at iteration number 14.
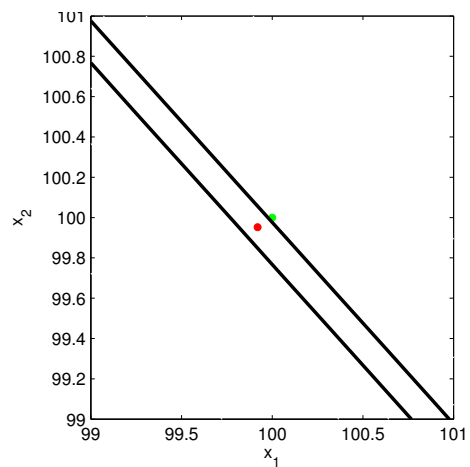
(b) Same as in Figure 8(a), zooming on x_{14}^+, and also showing (green) the true position $\tilde{x}_{true}$.
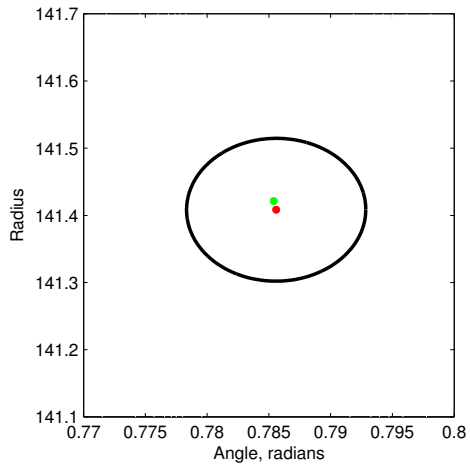
(c) (Black) 1-σ confidence area of the measurement variable z at iteration number 14. Red point corresponds to $\hat{z}_{14}$, and green point depicts $h(\tilde{x}_{true})$.
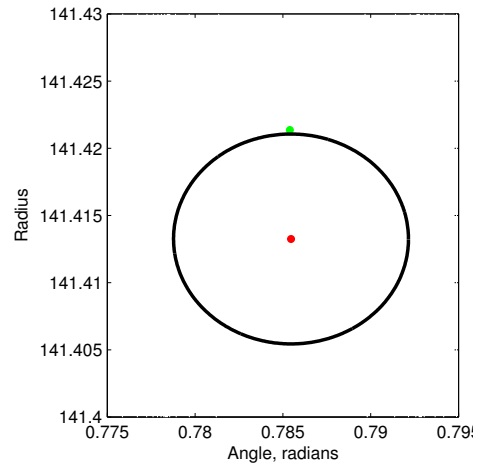
(d) Same as Figure 8(c) at iteration number 21.

Figure 8. Divergence process of the UKF.

In conclusion, the state covariance reduction appears to occur overly fast compared with the accuracy of the state estimates. The misalignment of the eigenvectors of $P_{xx,k}$, together with the high condition number of this matrix, leads the filter to a misinterpretation of new residuals. These two effects seem to lead the filter to ultimately diverge, as was described previously.

VI.A.   Modifications to the UKF

Based on the hypothesis that the divergence of the UKF is due to the over-reduction of the covariance matrix compared to the error reduction in the state estimate, we defined two types of filter modifications, one by increasing the measurement noise level as in the B-EKF and B-mtSOF strategies, and second, by using more information from new measurements in the residuals. The first modification is labeled B-UKF and the second modification UKFz.

VI.A.1.   B-UKF

Based on the results obtained examining bump-up strategies with the EKF, the bump-up UKF (B-UKF) is defined as follows

$$R_{new} = R + \sum_{i=0}^{2n} W_i^{(c)} (\mathcal{Z}_{i,k} - \hat{z}_k)(\mathcal{Z}_{i,k} - \hat{z}_k)^T$$

and

$$P_{zz,k,new} = R + 2 \sum_{i=0}^{2n} W_i^{(c)} (\mathcal{Z}_{i,k} - \hat{z}_k)(\mathcal{Z}_{i,k} - \hat{z}_k)^T$$

Results using these modifications are presented in Figure 9 together with a comparison with the original UKF. This figure shows that the B-UKF has delayed the divergence of the nominal UKF, though it does not eliminate the problem.

VI.A.2.   UKFz

The second modification alters the UKF algorithm by computing $\hat{z}_k$ as $h(\hat{x}_k^-)$ instead of using a high-order transformation. The rationale behind this approach is based on the results in Figure 7. That figure suggests that equation (23) is significantly more accurate than (10). For the same reason, the measurement residuals are smaller in the UKF than when using a linear approximation for the expected measurement computation. The residuals computed as $z_k - h(\hat{x}_k^-)$ are expected to point in a similar direction as the residual $z_k - \hat{z}_{k,ukf}$, but with a larger magnitude. Thus, $h(\hat{x}_k^-)$ should be nearly equivalent to an over-weighting of the new residuals in the state update equation, but without an increase in the contraction rate of the state covariance matrix. This strategy will be referred to as UKFz.

Figure 9 shows that the UKFz is the only approach that appears to avoid diverging at least for the experiment being considered. The convergence rate for this filter seems to be logarithmic (nearly linear in logarithmic scale), as was the case with the B-EKF strategies, though the UKFz is much faster. The figure shows that this filter reaches the numeric precision of the computer at the steady state very fast. Notice that the error at steady state is primarily due to the rounding errors associated to the computation of $\sqrt{P_{xx,k}^-}$.

VII.   Sensitivity Analysis

The results presented in the previous sections were based on a representative experimental configuration, also used by several authors in the past, and a particular choice of model parameters such as the true position, relative noise level, and a priori measurement error and uncertainty.

We thus performed an extensive set of numerical simulations to examine the dependence of these results on variations of these choice parameters. As part of this sensitivity analysis, we assessed filter performance for the following and wide range of variations:

- Initial covariance error:

$$P_0 = \begin{pmatrix} \sigma^2 & 0 \\ 0 & \sigma^2 \end{pmatrix}, \qquad \text{where } \sigma \in [10^{-8}, 10^8]$$
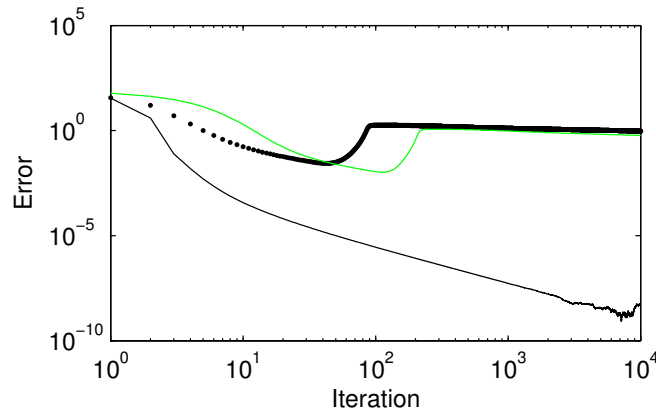
Figure 9. Variation of the state estimation error for the (black dots) UKF, (green line) the B-UKF, and (black line) the UKF-z strategies.

- Noise levels associated with different types of measurements:

$$R = \begin{pmatrix} 2.5\text{E-}5 + \beta & 0 \\ 0 & 6\text{E-}3 \end{pmatrix}, \qquad \text{where } \beta \in [0, 0.1]$$

- Error in the initial estimate ($= \hat{x}_0 - \tilde{x}_{true}$):

$$\hat{x}_0 = \tilde{x}_{true} + d \cdot (\cos\alpha, \sin\alpha)$$

  – for a fixed distance (angular variations): $\alpha \in [0, 2\pi), d = 82.4621$
  – for a fixed angle (distance variations): $\alpha \in \{0, \pi/4\}, d \in [10^{-11}, 10^4]$.

To be fully consistent with previous sections and enable direct comparison, the true position was always assumed to be at $\tilde{x}_{true} = (100, 100)$, the vehicle was static (i.e., $\dot{x} = f(t, x) = 0$), and there was no process noise ($Q \equiv 0$). This investigation does not include the effect of using different values for $\tilde{x}_{true}$ because this can be readily derived from the analysis of previous terms. A variation of the true state $\tilde{x}_{true} \neq (0, 0)$[a] is equivalent to a rotation and dilation of the state space. Therefore, the analysis of a variation on the true state can be derived from the analysis of a variation on the initial estimate and the covariance matrix magnitude.

We defined an indicator I of the filter performance to facilitate comparisons among the filters. It is defined as the ratio between the error at iteration number 1000, when the filters should have already reached steady state, and the initial error:

$$I = \frac{||\hat{x}_{1000} - \tilde{x}_{true}||}{||\hat{x}_0 - \tilde{x}_{true}||} \tag{27}$$

This parameter is thus an indicator of the error reduction, or improvement of the initial estimate, i.e., lower values of I correspond to larger improvements.

Figure 10 shows the improvement for the four types of analysis proposed above. Most of the filters (i.e., EKF, B-EKF 3 and 4, mtSOF, B-mtSOF, UKF, B-UKF) do not perform well regardless of the magnitude of the initial state covariance (see Figure 10(a)). The exception are filters B-EKF 1 and 2, and UKFz. In those cases, results suggest that it is important to start with a coherent P_0 covariance matrix to get good estimation performance (i.e., $\tilde{x}_{true}$ should be inside the 1-σ confidence area defined by $\hat{x}_0$ and P_0). If the initial covariance matrix is big enough, all three filters reach the computer numerical precision associated with the algorithm (the precision for the UKFz is worse than the B-EKF 1 and 2, primarily because of the computation of $\sqrt{P_{xx,k}^-}$). Otherwise, the filter is over-constrained and has no ability to improve the state estimate, as intended.

---

[a]The measurement model derivative does not exist at $(0, 0)$, and will be excluded from the configuration set for $\tilde{x}_{true}$.

Figure 10(b) shows the existing dependence on noise levels for several filters. For these filters, there appears to be a small interval of noise ratios in which filter performance is sensitive. The two noise levels can be considered comparable when $\sigma_{distance} \approx ||x|| \sin(\sigma_{angle})$. For the experiments performed $||x|| \approx 100$, and noises will be comparable when, $\sigma_{distance} \approx 100 \, \sigma_{angle}$. When the noise levels on the angular measurements are larger ($\sigma_{distance} \ll 100 \, \sigma_{angle}$), EKF, mtSOF, and UKF seem to diverge as in Sections V–VI. When the noise levels of the radial measurement are the largest ($\sigma_{distance} \gg 100 \, \sigma_{angle}$), the state estimate uncertainty is much larger in the radial direction than in the angular direction. This situation reduces the convergence speed in the radial direction (vs. the speed in the angular direction). As a result, the orientation of the eigenvectors of the state covariance will vary little after a few iterations compared with the example in Section III. This indicates that when noise ratios are higher than $\sim$0.08, the UKF does not diverge. From this figure, the effect of the bump-up on the UKF is to reduce the impact of higher angle noise levels of the measurements. The same phenomenon occurs with the bump-up mtSOF when compared to the mtSOF. Performance of B-EKF, and UKFz strategies appear to be independent of the ratios between measurement noise levels.

Figure 10(c) shows that the performance of EKF, B-EKF 1-4, and UKFz vary as a function of the initial direction α. If $\hat{x}_0$ has the same angle as $\tilde{x}_{true}$, i.e. $\hat{x}_0 = \tilde{x}_{true} + (r \cdot \cos(\pm\pi/4), r \cdot \sin(\pm\pi/4))$, a filter only needs to improve the magnitude of the initial state, not the angle θ. This configuration ($\alpha = \pm\pi/4$), in fact, provides the best filter performance. The rest of the filters (mtSOF, B-mtSOF, UKF, and B-UKF) do not perform well regardless of the angle. In the case of the UKF, this fact highlights the high sensitivity of the filter on small variations of the measurement correlation matrix $P_{zz,k}$, that make the filter diverge even in the case that $\hat{x}_0$ and $\tilde{x}_0$ have the same angle (situation corresponding to $\alpha = \pm\pi/4$). In such a case, the small variations on the measurement correlation matrix are mainly due to the rounding errors in the computation of $\sqrt{P_{xx,k}^-}$.

In order to address the filter performance as a function of the initial distance r while being consistent with the conclusions regarding the analysis of the initial state covariance matrix, a different covariance matrix was considered for each initial state $\hat{x}_0 = \tilde{x}_{true} + (r \cdot \cos(\alpha), r \cdot \sin(\alpha))$. For each distance r, we chose $P = \sigma^2 I$, where $\sigma = 2.5r$, which guarantees that the true state is inside the initial confidence area. The performance curve of the filters in Figures 10(d) and 10(e) shows an unexpected pattern: when the initial estimate is close to the true state, the filter is unable to improve the initial error. This behavior is the subject of ongoing research.

VIII.   Conclusions

We investigated the divergence problems of Kalman-type filters in the presence of nonlinearities for the EKF, high-order filters (mtSOF), and LRKF families (UKF). In particular, this work fully isolated the characteristics of the prediction and update phases of these filters and concentrated on the update phase by associating the nonlinearities exclusively to the measurement models. Measurements were modeled for two independent sensors with contrasting levels of accuracy. This type of investigation on sensor fusion is relevant for multi-satellite missions that rely on formation flying technologies.

It was determined that not only the EKF, but also the mtSOF and UKF may diverge, and that there is a common cause for the divergence of all these filters for the experimental confiuration considered. When using nonlinear measurement models, the accuracy of the state update equation is not commensurate with the reduction of the state covariance during the update phase. In the case of the EKF and UKF, the misalignment between the eigenvectors of the state covariance matrix is interpreted by the filter as a correlation between the measurements. This effect plays an important role in the divergence process.

We designed several modifications to these filters were proposed to circumvent the over-reduction of the state covariance without increasing the computational load over that of the baseline algorithms. The strategies were primarily based on a bump-up of the covariance matrix of the measurement noise. Those defined by equations (13) and (15) provided good performance when applied to the EKF, but did not eliminate divergence in the mtSOF and UKF. The accuracy of the measurement residuals or innovations was found to be key to the performance of the UKF. An additional modification was proposed to increase the importance of the residuals in the update phase (UKFz). This filter clearly outperforms all of the other filters investigated.

We performed a numerical study to examine the dependence of the filter performance on a priori filter information for key filter parameters such as $\hat{x}_0$, $P_{xx,0}$, and R. This study was intended to identify the set
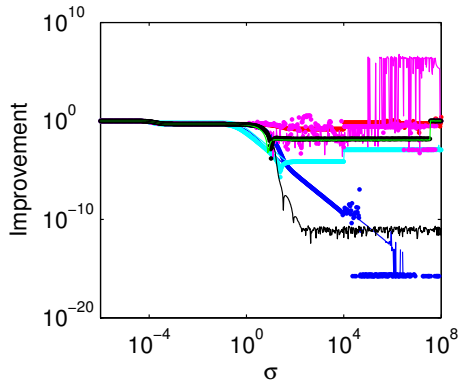
(a) Sensitivity on σ ($P = \sigma^2 I$). The initial error in distance is 82.46, therefore, σ should be larger than this value in order for the 1-σ confidence area to contain the true state.
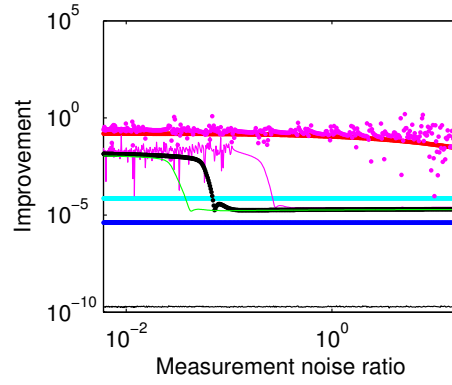
(b) Sensitivity on measurement noise levels ratio $\frac{\sigma_r}{\sigma_\theta}$.
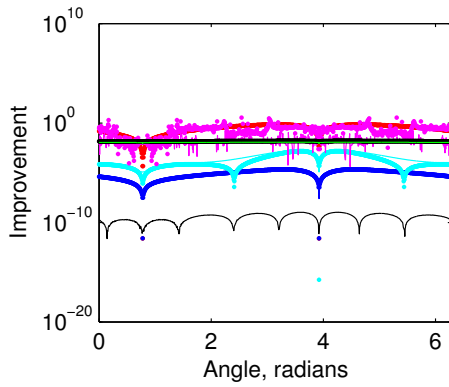
(c) Sensitivity on angle (α) variations.
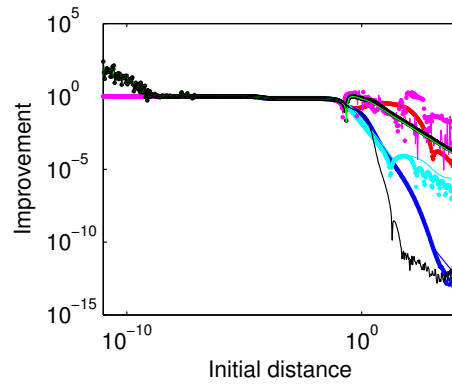
(d) Sensitivity to initial distance (d) in the horizontal direction ($\alpha = 0$).
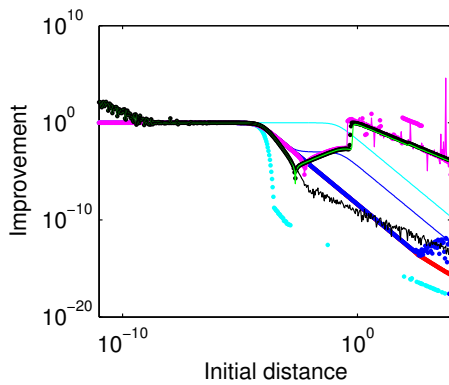
(e) Sensitivity to initial distance (d) in the same direction of x_0 ($\alpha = pi/4$).
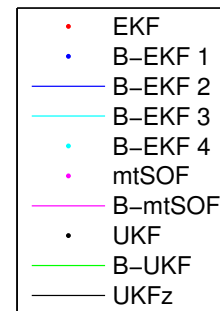
Figure 10. Variation of the state estimation error for various filters and experimental configurations.

of possible configurations that led previous filters to diverge, and to test the filters and filter modifications under a wide set of configurations. For most of the configurations tested, the divergence problems observed in the baseline experimental configuration remained. The filters that provide the best performance and that overcome the divergence problem were the B-EKF 1, B-EKF 2, and the UKFz. The UKFz was the fastest filter to reach steady-state and also showed excellent estimation performance.

IX.   Acknowledgments

References

[1]Borde, J., Teston, F., Santandrea, S., and Boulade, S., "Feasibility of the PROBA 3 formation flying demonstration mission as a pair of microsats in GTO," 55th International Astronautical Congress of the International Astronautical Federation, the International Academy of Astronautics, and the International Institute of Space Law, Oct. 2004.

[2]Geller, D., "Linear Covariance Techniques for Orbital Rendezvous Analysis and Autonomous Onboard Mission Planning," AIAA Journal of Guidance, Control and Dynamics, Vol. 29, No. 6, 2006, pp. 1404–1414.

[3]Scharf, D., Ploen, S., and Hadaegh, F., "A Survey of Spacecraft Formation Flying Guidance and Control (Part I): Guidance'," American Control Conference, 2003.

[4]Gelb, A., Applied Optimal Estimation, MIT Press, 1974.

[5]Ristic, B., Arulampalam, S., and Gordon, N., Beyond the Kalman filter: particle filters for tracking applications, Artech House, Boston, MA, 2004.

[6]Huxel, P. J. and Bishop, R. H., "Fusing inertial and relative range measurements for inertial navigation in the presence of large state error covariances," 16th AAS/AIAA Space Flight Mechanics Conference, 2006.

[7]Plinval, H., Analysis of Relative Navigation Architectures for Formation Flying Spacecraft, Master's thesis, Dept. of Aeronautics and Astronautics, Massachusetts Institute of Technology, Feb. 2006.

[8]Mandic, M., Distributed Estimation Architectures and Algorithms for Formation Flying Spacecraft, Master's thesis, Dept. of Aeronautics and Astronautics, Massachusetts Institute of Technology, June 2006.

[9]Brown, R. G. and Hwang, P. Y. C., Introduction to random signals and applied Kalman Filtering, John Wiley & Sons, 1992.

[10]Ferguson, P. and How, J., "Decentralized estimation algorithms for formation flying spacecraft," AIAA Guidance, Navigation and Control Conference, 2003.

[11]Bellaire, R. L., Kamen, E. W., and Zabin, S. M., "A new nonlinear iterated filter with applications to target tracking," SPIE Signal and Data Processing of Small Targets Conference, 1995, pp. 240–251.

[12]Haykin, S., The Unscented Kalman filter: Kalman filtering and neural networks, Wiley, 2001.

[13]Julier, S. and Uhlmann, J. K., "A New Extension of the Kalman Filter to Nonlinear Systems," 1999.

[14]Lefebvre, T., Bruyninckx, H., and Schutter, J. D., "Kalman filters for non-linear systems: a comparison of performance," International Journal of Control, Vol. 77, No. 7, 2004.

[15]Maybeck, P. S., Stochastic Models, Estimation and Control, New York, NY: Academy Press, 1982.

[16]Mitchell, M. L., CDGPS-Based Relative Navigation for Multiple Spacecraft, Master's thesis, Dept. of Aeronautics and Astronautics, Massachusetts Institute of Technology, June 2004.

[17]Nash, J. and Walker-Smith, M., Nonlinear Parameter Estimation an Integrated System in BASIC, New York: Marcel Dekke, 1987.

[18]der Merwe, R. V. and Wan, E., "The Square-Root Unscented Kalman Filter for State and Parameter Estimation," International Conference on Acoustics, Speech, and Signal Processing, 2001.

[19]Julier, S., Uhlmann, J., and Durrant-Whyte, H. F., "A new method for the nonlinear transformation of means and covariances in filters and estimators," Automatic Control, IEEE Transactions on, Vol. 45, No. 3, March 2000, pp. 477–482.

[20]Beichman, C., "The Terrestrial Planet Finder - The search for life-bearing planets around other stars," Astronomical Interferometry Meeting, 1998, pp. 719–723.

[21]Lefebvre, T., Bruyninckx, H., and Schuller, J. D., "Comment on "A new method for the nonlinear transformation of means and covariances in filters and estimators" [and authors' reply]," Automatic Control, IEEE Transactions on, Vol. 47, No. 8, Aug. 2002, pp. 1406–1409.

[22]Julier, S. and Uhlmann, J., "Unscented Filtering and Nonlinear Estimation," No. 3, IEEE, 2004.

RELATIVE FORMATION FLYING DYNAMICS AND CONTROL OF A TWO-ELEMENT VIRTUAL TELESCOPE ON A HEO

Laura Perea[1], Simone D'Amico[2], Pedro Elosegui[1]

[1] *Instituto de Ciencias del Espacio (CSIC) & Institut d'Estudis Espacials de Catalunya (IEEC), Edifici Nexus, c/Gran Capità 2–4, 08034 Barcelona, Spain, perea@ice.csic.es, pelosegui@ice.csic.es.*
[2] *Deutsches Zentrum für Luft- und Raumfahrt (DLR), 82230 Wessling, Germany, simone.damico@dlr.de.*

ABSTRACT

The goal of this study is to find an appropriate control law for a constellation of two spacecraft in flight formation that constitutes a virtual telescope for Sun's corona observation. During scientific operations, both satellites should be aligned with the Sun, thus, one of the spacecraft projects its shadow to the other while orbiting the Earth on a High Eccentricity Orbit. This mission characteristic has a direct impact on the relative dynamics, since the relative Solar Radiation Pressure between spacecraft has a higher effect on the dynamics than the Earth's gravity harmonics and the Sun and Moon perturbations. Based on this result, we explore the applicability and performances of several continuous controls based on pole placement techniques.

1. INTRODUCTION

Formation flying is a key, forthcoming technology with an ever increasing number of applications in space missions. Interest for these missions resides on the idea that several small and coordinated spacecraft may minimize the cost of a mission, lower its risk by implementing redundancy and robustness, and enable scientific applications, particularly involving long baselines, that are not feasible with a single monolithic spacecraft. Although significant progress has been made over the last years, critical technological challenges still remain in areas such as navigation and control, on-board sensing and actuation, high-level mission management and planning, distributed fault-detection, isolation, and recovery. Moreover, failure and termination of past formation flying missions such as DART and TechSat-21 have hindered progress in this area.[1] However, the success of more recent missions such as OrbitalExpress and the advanced state of upcoming missions such as PRISMA and TanDEM-X, offer a positive outlook for these technologies.

PROBA-3 is a significant step forward in the roadmap of formation flying technologies and a leap to advanced missions such as Xeus and Darwin. The main objective of PROBA-3 is to test and validate formation acquisition and tight formation keeping on a High Eccentricity Orbit (HEO) around the Earth. As scientific payload, PROBA-3 will carry a solar coronagraph which, during scientific observations, requires constant alignment with the axis of the Sun's shadow casted by an eclipsing spacecraft. A tight formation will be kept during the apogee passage, but spacecraft will be in free-flying mode during the perigee passage to minimize energy costs associated with the cancellation of orbit perturbations.

The aim of this study is to analyze the relative dynamics between two spacecraft under mission characteristics similar to PROBA-3, and design a suitable control law for formation

acquisition and formation keeping. The main control law will be based on an approximation of the relative dynamics plus a time-invariant linear term. Several options for tuning this linear term will be considered such as the Linear Quadratic Regulator (LQR) solution based on suitable approximations of the relative dynamics. The resulting controls will be compared using numerical simulations under a PROBA-3-like scenario.

2. DYNAMICS

In accordance with PROBA-3, our study involves two spacecraft in close proximity whereby the Sun's radiation arriving to one of the spacecraft is eclipsed by the other, together acting as a two-element, virtual telescope, as depicted in Fig. 1. For the definition of the relative dynamics of such telescope, we will assume that the eclipsing spacecraft, shaped as an occulter disk, follows a natural trajectory on a HEO around the Earth. The spacecraft that carries the scientific sensor, an optical coronagraph, is required to be aligned with the axis of the Sun's shadow casted by the occulter disk. Furthermore, the baseline between the two spacecraft is to be kept at a fixed distance. In the following, these satellites will be referred to as the occulter spacecraft and the coronagraph spacecraft, respectively, to ease identification.
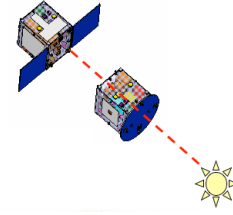
Fig. 1: PROBA-3 scheme. Source: ESA.

2.1 Dynamics of the coronagraph spacecraft

The requirement of alignment between the Sun, and the occulter and coronagraph spacecraft can be defined as

$$x_{cs,ref} = x_{os} + l \left(\frac{x_{os} - x_{\odot}}{||x_{os} - x_{\odot}||} \right) \tag{1}$$

where x and v denote position and velocity, respectively, of the centre of mass of a spacecraft in a Geocentric Inertial (GCI) reference frame; the subscripts os and cs refer to the occulter and coronagraph spacecraft, respectively; the subscript cs, ref refers to the reference trajectory of the coronagraph; l is the reference separation between the occulter and the coronagraph spacecraft; and $\odot$ is the Sun's symbol.

Therefore, the equations for the relative motion of the coronagraph spacecraft with respect to its reference orbit are

$$\dot{x}_{cs} - \dot{x}_{cs,ref} = v_{cs} - v_{os} - l \left(\frac{x_{os} - x_{\odot}}{||x_{os} - x_{\odot}||} \right)'; \tag{2}$$

$$\dot{v}_{cs} - \dot{v}_{cs,ref} = f(x_{cs}) - f(x_{os}) - l \left(\frac{x_{os} - x_{\odot}}{||x_{os} - x_{\odot}||} \right)'' + u \tag{3}$$

where $f(x)$ is the natural acceleration of x; $(\cdot)'$ and $(\cdot)''$ denote the first and second time derivative of the function within brackets, respectively; and u is the control input.

The difference between the coronagraph spacecraft with respect to its reference trajectory will be referred to as the control error, and be denoted by $e_c := (x_{cs} - x_{cs,ref}, v_{cs} - v_{cs,ref})^T$.

The term $f(x_{cs}) - f(x_{os})$ represents the relative acceleration between two free-flying satellites separated by l meters, and it is the sum of several relative forces acting simultaneously,

$$f = f_{CM\oplus} + f_{sh,n>0} + f_{SRP} + f_{CM\odot} + f_{CM_M} + f_{drag} + f_{others}, \tag{4}$$
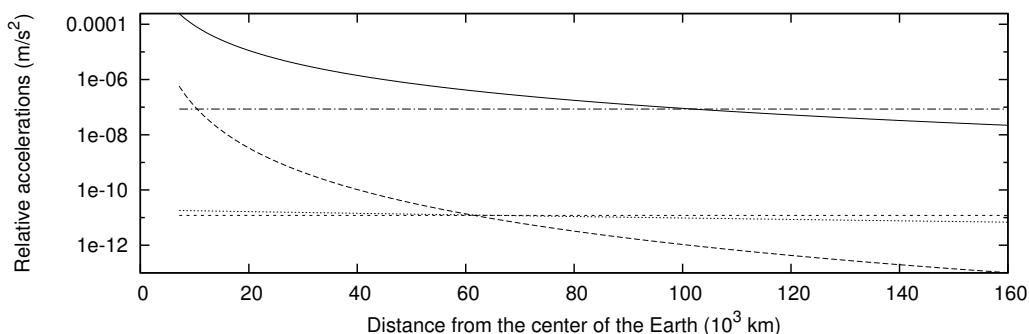
Fig. 2: Relative accelerations between two satellites aligned with the Sun-Earth axis, at a constant separation of 150 m. Contributions are from (continuous line) Earth's gravity constant, (long dashed line) high-order geopotential, (short dashed line) Sun's gravity constant, (dotted line) Moon's gravity constant, and (dotted-dashed line) SRP.

where $f_{CM\oplus}$, $f_{CM\odot}$, and f_{CM_M} stand for the contribution due to Earth, Sun and Moon gravity constants respectively, $f_{sh,n>0}$ is the contribution due to the spherical harmonics of positive order ($n > 0$) of the geopotential, f_{SRP} is the Solar Radiation Pressure (SRP) contribution, f_{drag} is the atmospheric drag contribution, and f_{others} stands for the rest of lower-order contributions such as tides, albedo, and relativity. Fig. 2 shows, for an inter-satellite separation of 150 m, the magnitude of the relative acceleration of the most significant forces as a function of the distance to Earth, which is largely characterized by the contributions from the Earth gravity constant and the SRP coefficients. It is interesting to note that, in contrast to what happens for the rest of the forces, the relative force due to the SRP can be of similar magnitude than the SRP of the occulter. Under the virtual-telescope configuration, the occulter is under full illumination while the coronagraph is in dark penumbra due to the occulter's shadow, which result in a relative SRP with the same order of magnitude than the SRP of the occulter. (See section 4.1 for departures from this configuration.)

The term $l \left(\frac{x_{os}-x_\odot}{||x_{os}-x_\odot||} \right)''$ is due to the rotation of the coronagraph with respect to the occulter necessary to keep the former aligned with the Sun-occulter axis. This rotation is almost equivalent to the rotation of the Earth around the Sun except for slight variations on the unit vector $\left(\frac{x_{os}-x_\odot}{||x_{os}-x_\odot||} \right)$ due to the spacecraft orbit around Earth. Thus, it has a 1-year period, and its second derivative is of the order of $l \times 10^{-15}$ m/s^2.

2.2 The effect of the coronograph shadow model on the relative dynamics

The formulation of the relative acceleration due to the SRP is

$$
\begin{aligned}
f_{SRP}(x_{cs}) - f_{SRP}(x_{os}) &\approx P_\odot AU^2 \left[\nu(x_{cs})\varphi_{os}(x_{cs})K_{cs} - \nu(x_{os})K_{os} \right] \frac{x_{os} - x_\odot}{||x_{os} - x_\odot||^3} \\
&\approx \nu(x_{os})P_\odot AU^2 \left[\varphi_{os}(x_{cs})K_{cs} - K_{os} \right] \frac{x_{os} - x_\odot}{||x_{os} - x_\odot||^3} \quad (5)
\end{aligned}
$$

where $P_\odot \approx 4.56 \cdot 10^{-6}$ N/m^2 is force per unit area exerted by the SRP; $\nu(x) \in [0,1]$ is the Earth-shadow coefficient; $\varphi_{os}(x) \in [0,1]$ is the a coefficient to account for the shadow projected by the occulter spacecraft; K_{os} and K_{cs} are the ratios $C_R A/m$ for the occulter spacecraft and the coronagraph, respectively; C_R is the radiation pressure coefficient of the satellite surface;
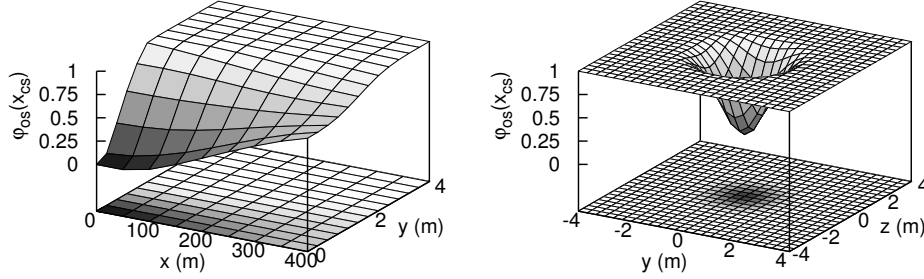
Fig. 3: Illumination coefficient $\varphi_{os}(x_{cs})$. The results are plotted in an orthonormal reference frame centered at x_{os}. The $x-$axis is aligned with the shadow direction. The $y-$, and $z-$axis represent the distance to x_{os} in two arbitrary directions perpendicular to the shadow axis.

A is the area of Sun exposition; m is the mass of the spacecraft (both A and m are assumed constant values); $x_{\odot}$ is the position vector of the Sun; and AU is the astronomical unit.

When the coronograph is in dark penumbra, the φ_{os} is close to 0 and the relative SRP acceleration becomes close to the acceleration of the occulter, as discussed above and shown in Fig. 2. Any significant variation of the relative SRP over short-time intervals arises from variations in φ_{os}, i.e., the eclipse conditions. We discuss hereafter a model for the shadow of the occulter on the coronograph.

Unlike Earth's shadow on the spacecraft, the shadow projected by a satellite is very narrow and the assumption of constant illumination (or lack thereof) on the Sun-facing surface of the shadowed spacecraft breaks down. More realistically, the coronograph surface could experience almost the whole gamut Sun exposure, from dark penumbra to full illumination, depending on the relative spacecraft positions. The acceleration of the coronagraph spacecraft due to the pressure exerted by the solar radiation can be mathematically modelled as

$$f_{SRP}(x_{cs}) = \frac{1}{|S|} \int_S \eta(x) a_{srp}(x) dx \tag{6}$$

where S is the region of the spacecraft facing the Sun, $x \in S$, $\eta(x) \in [0,1]$ is the eclipse coefficient corresponding to the occulter shadow, and $a_{srp}(x)$ is the acceleration of the spacecraft due to the SRP assuming there is no spacecraft shadow. The eclipse coefficient has its minimum value when the coronagraph is aligned with the shadow axis of the occulter, and has its maximum value of 1 when it is far enough from this axis. The two views in Fig. 3 illustrate the eclipse coefficient function for an occulter disk, which is constant outside the shadow area and is dome shaped over a cross section perpendicular to the shadow axis.

3. CONTROL DEFINITION

In this section, we will present different approaches to define a suitable control law for a virtual telescope that has to be aligned with the Sun. In order to guarantee convergence of the expected formation and, once achieved it, keep it with a high level of accuracy (of the order of the centimeter), we will assume that the control u can be executed at high frequencies (≥ 1 Hz). Therefore, the control laws that are presented will be defined as continuous functions.

Inspection of Eq. (3) reveals that, once the formation has converged, the thrust necessary to

continuously keep the formation assuming an infinite accuracy should be

$$u = f(x_{os}) - f(x_{cs}) + l \left(\frac{x_{os} - x_{\odot}}{||x_{os} - x_{\odot}||} \right)''. \tag{7}$$

However, some limitations have to be considered for a realistic definition of the control thrust. The physical thrust limitations, such as the maximum thrust, the thrust resolution, and the (high-frequency) discrete execution of the control input should be accounted for, together with the numerical errors such as the model inaccuracies, and the discrete computation of the control input. For example, the magnitude of the acceleration of the Sun with respect to the occulter $l(\cdot)''$ is of the order of $l \times 10^{-15} \ m/s^2$ which is, for short baselines, under the thrust resolution of the state-of-the-art thrusters. Therefore, this term will be dropped from Eq. (7) and, instead, contribute to its numerical inaccuracy.

All these physical limitations and numerical inaccuracies of the system could lead to the violation of the formation requirements rather quickly. For this reason, an additional term should be included in the control law to guarantee smooth convergence towards the desired formation. A technique commonly employed for motion stabilization is to introduce a linear term which formally guarantees exponential convergence of the system to the desired formation,

$$u = f(x_{os}) - f(x_{cs}) + K_H \cdot e_c, \quad K_H = (H_1, H_2) \in \mathbb{R}^{3 \times 6}. \tag{8}$$

Using this formulation, the system (2)-(3) reduces to

$$\dot{e}_c = H \cdot e_c, \qquad H = \begin{pmatrix} 0 & I_3 \\ H_1 & H_2 \end{pmatrix} \in \mathbb{R}^{6 \times 6}, \tag{9}$$

which guarantees exponential convergence to the reference trajectory as long as the stabilization matrix H is Hurwitz, i.e., the real part of the eigenvalues of H is negative. The speed of convergence of the system depends on these eigenvalues, aka poles in the engineering literature. The larger these values, the faster the convergence. However, large values may result in thrust saturation. Finding suitable values for these parameters is a non-unique procedure. One approach involves testing different indicators for a wide range of configuration values using numerical simulations. In what follows, we will present three different strategies to tune the pole placement of system (9) assuming different approximations of the relative dynamics.

3.1 Nonlinear control

We approximate the relative dynamics by considering only the Earth's gravity and the SRP contributions to model the relative acceleration (see 2.1).

$$
\begin{aligned}
u \quad := \quad & GM_{\oplus} \left(\frac{x_{cs} - x_{os}}{||x_{os}||^3} \right) \\
& + \nu(x_{os}) P_{\odot} AU^2 \left(\varphi_{os}(x_{cs}) K_{cs} - K_{os} \right) \frac{x_{\odot} - x_{os}}{||x_{\odot} - x_{os}||^3} \\
& + K_H \cdot \begin{pmatrix} x_{cs} - x_{cs,ref} \\ v_{cs} - v_{cs,ref} \end{pmatrix}
\end{aligned} \tag{10}
$$

Due to the non linear characteristics of the model for the relative dynamics, we will refer to this control function as the nonlinear control.

In order to guarantee the continuous formation convergence, we will consider the following Hurwitz matrix for the present control

$$H = \begin{pmatrix} 0 & I_3 \\ -\alpha I_3 & -\beta I_3 \end{pmatrix} \qquad \text{with} \qquad \alpha, \beta > 0.$$

The poles of the resulting closed loop system are shown in Fig. 4. The α value acts as a weight of the relative positions within the controller, while β weights the relative velocity. Therefore, large β values will result in position variations that hardly depend on the relative positions, but highly depend on the relative velocities. As a result, the convergence to the reference position will be slow and with few oscillations. On the contrary, large α values will result in fast movements towards the reference position with large relative velocities. At the instant the spacecraft reaches the reference position, the relative velocity may be too large and the relative position may thus increase again before the controller can cancel the relative velocities. This behavior could even lead to error oscillations with amplitudes that increase with time, specially, though not only, in the case of thrust saturation. In this study, the proper tuning of the α and β values will be done by comparing the performances of different configuration values using numerical simulations.
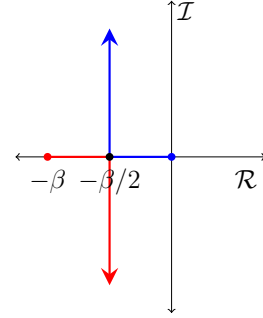
Fig. 4: Poles of the closed loop system when using the nonlinear control: $\frac{-\beta \pm \sqrt{\beta^2 - 4\alpha}}{2}$. Blue and red lines denote the variation of the poles as $\alpha \geq 0$ increases for a given β value.

3.2 Robust pole placement control

In previous sections, we have presented a control function that moves the poles of the system to the desired location by considering a nonlinear approximation of the dynamics. In this sub-section, we will consider an additional common technique: the robust pole assignment algorithm designed by Kautsky-Nichols-Van Dooren (KNV) in [2], and implemented as the Matlab[©] built-in function *place*. The KNV algorithm optimizes the choice of the eigenvectors for a robust, or well-conditioned, solution for a given set of poles. In order to use this method, we need to consider a linear and time-invariant approximation of the system (2)-(3).

As discussed before, the second derivative of the Sun-rotation term in Eq. (3) can be neglected, and the relative dynamics are mainly characterized by the Earth gravity and the differential SRP. The Earth gravity contribution can be easily approximated by a first order polynomial in e_c assuming that $||x_{os}||^3$ is almost constant in the time frame of several hours as
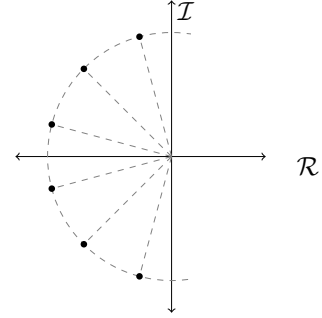
Fig. 5: Pole placement of a closed loop system after the KNV algorithm control (see text).

$$\begin{aligned} f_{CM}(x_{cs}) - f_{CM}(x_{os}) & \approx -\frac{GM_\oplus}{||x_{os}||^3}(x_{cs} - x_{os}) \\ & = \frac{GM_\oplus}{||x_{os}||^3}(x_{os} - x_{cs,ref}) - \frac{GM_\oplus}{||x_{os}||^3}(x_{cs} - x_{cs,ref}) \end{aligned} \qquad (11)$$

When the coronagraph is close to its reference position, the independent coefficient of this polynomial is larger than the drift, however, a linear model omits it.

The linearization of the relative SRP presents additional difficulties. According to Eq. 5, an approximation of the relative SRP around the reference trajectory needs to include a non-zero constant term, unless $K_{cs} = K_{os}\varphi_{os}(x_{cs,ref})$. The linear term would come from the linearization of the eclipse coefficient $\varphi_{os}(x_{cs})$ around $x_{cs,ref}$. Because of the dome shape of the eclipse

coefficient, as observed in Fig. 3, the gradient is 0 in any direction perpendicular to the shadow axis. Thus, the derivative is only nonzero in the direction of the shadow axis. We will denote $\mathcal{L}_{u_\odot}\varphi_{os}$ the derivative of φ_{os} in this unique direction, or Lie derivative

$$\mathcal{L}_{u_\odot}\varphi_{os} = \frac{\partial \varphi_{os}}{\partial x} \cdot u_\odot$$

where $u_\odot = \frac{(x_{os} - x_\odot)}{||x_{os} - x_\odot||}$ is an unitary vector in the shadow direction. The eclipse coefficient can be approximated by,

$$\varphi_{os}(x_{cs}) \approx \varphi_{os}(x_{cs,ref}) + \mathcal{L}_{u_\odot}\varphi_{os}\, u_\odot^T\, (x_{cs} - x_{cs,ref}), \qquad (12)$$

and the relative SRP by,

$$f_{SRP}(x_{cs}) - f_{SRP}(x_{os}) = \nu(x_{os})P_\odot AU^2\left(\varphi_{os}(x_{cs,ref})K_{cs} - K_{os}\right)\frac{x_\odot - x_{os}}{||x_\odot - x_{os}||^3}$$
$$+\nu(x_{os})P_\odot AU^2 K_{cs}\mathcal{L}_{u_\odot}\varphi_{os}\, u_\odot^T\, \frac{x_\odot - x_{os}}{||x_\odot - x_{os}||^3}(x_{cs} - x_{cs,ref}). \qquad (13)$$

In general, the relative SRP at the reference position, or the constant term, is larger than the variation of this differential acceleration due to the linear term, which depends on $\mathcal{L}_{u_\odot}\varphi_{os}$. For this reason, the error of a linear approximation (without the constant term) is of the same order, as the error of omitting the full contribution of the relative SRPs.

Therefore, a linear approximation of the dynamics will not include the constant term of the Earth gravity contribution and the relative SRP. The following equation describes the resulting linear approximation according to previous discussion,

$$\dot{e}_c = A_c e_c + Bu, \qquad (14)$$

with

$$A_c = \begin{pmatrix} 0_3 & I_3 \\ -\frac{GM_\oplus}{||x_{os}||^3}I_3 & 0_3 \end{pmatrix} \qquad \text{and} \qquad B = \begin{pmatrix} 0 \\ I_3 \end{pmatrix}.$$

In order to apply the KNV algorithm, we need to further assume time-invariance of the system. For this reason, we will split the orbit into several arcs and assume time-invariance of the system along each one of these arcs. The time length for these time windows depends on the rate of variation of the position vector norm, thus, on the period and eccentricity of the orbit. The linear time-invariant approximation to the relative dynamics enables the use of the KNV algorithm, obtain a control feedback matrix K_K, and define a linear control $u = K_K e_c$.

In what follows, we will define the poles of the closed loop system, to feed the KNV, at

$$bandwidth \cdot e^{2\pi i(j/12 + 5/24)} \qquad \text{with } j = 1 \div 6,$$

i.e., equally spaced along a circle of radius $bandwidth$ and restricted on the negative side of the complex plane as shown in Fig. 4. The resulting control will be referred to as KNV control.

3.3 Linear Quadratic Regulator control

In this section, we present a more sophisticated technique to define the control feedback matrix K which is based on the optimization of the ratio between the control errors and the energy cost associated to the control. This strategy, which is referred to as the Linear Quadratic Regulator, provides a linear control and shifts the indetermination of previous α and β values, or the

definition of the poles in the KNV control, to the indetermination of two weight matrices, Q and R, which provide a better insight into physics.

The objective of the LQR is to find a control u that minimises a potential function, also referred to as the cost function,

$$J \quad := \quad \int_{t_0}^{T_1} (u^T R u + e_c^T Q e_c) dt \tag{15}$$

where R and Q are positive definite matrices.

Then, the optimal control is of the form

$$u \quad = \quad -K_L e_c, \tag{16}$$

where $K_L = R^{-1} B^T P$ is the control gain or feedback matrix, and P is a symmetric non-negative definite matrix that satisfies the matrix Riccati equation. In a time-invariant system, the solution will reach a steady state after certain time, and the confidence matrix P will get close to a constant value. After convergence to the steady-state solution, $\dot{P} \approx 0$, and P can be computed as the solution of the Continuous Algebraic Ricatti Equation (CARE):[3–5]

$$0 = Q - PBR^{-1}B^T P + PA + A^T P, \tag{17}$$

In order to use this method, we will consider the same time-invariant linear approximation of the relative dynamics of Eq (14). This enables the use of the LQR solution to obtain a control feedback matrix K_L, and define a linear control $u = K_L e_c$. Since the 3×3 blocks of the dynamic matrix A_c are diagonal, and the correlations in the observations have been omitted, the resulting feedback gain matrix K_L of the LQR is of the same form as in the nonlinear control, $(a\,I_3 \quad b\,I_3)$ for certain $a, b \in \mathbb{R}$. The main appeal of the LQR strategy is the optimum selection of the parameters a and b with respect to the cost function J.

4. SIMULATIONS

4.1 Experimental Scenario

In order to exemplify the performances of previous control laws, we have defined a scenario for numerical testing of performances and comparison between different controls. This scenario is based on the formation flying mission of the European Space Agency PROBA-3. The reference orbit for this mission will be a HEO to avoid perturbances of the relative dynamics during the apogee passage, when the telescope is assumed to be active (see Fig. 6). During Sun's corona observations, both spacecraft should be aligned with the Sun, and they should preserve a baseline distance of 150 m to constitute the virtual telescope. In the present study, we have considered two baseline orbits: a more eccentric orbit with a period of three days and a less eccentric one with a period of one day, as they were preliminary contemplated for this mission. The Keplerian parameters of these two orbits have been included in Table 1. We have assumed that the sun-facing surface of the satellites are discs of radius R_{os}, and R_{cs}, respectively. The spacecraft physical characteristics used in current simulations have been summarized in Table 2. The metrology system is assumed to provide two modes of operations,
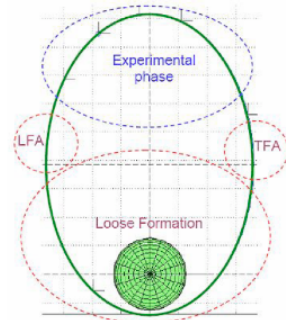

Fig. 6: PROBA-3 orbit passages scheme. Source: ESA.

8 of 15

Coarse and Fine, with lateral accuracy of 1 degree and 1 arcsecond, respectively, in standard deviation. The errors in longitudinal direction are assumed to be 1 cm in both navigation modes. Observations are collected at 1 Hz in coarse mode, and at 10 Hz in fine mode. The thrusters are assumed to reach 0.04 N before saturation, with maximum thrust resolution of 10^{-6} N.[6]

Orbit name	a (km)	e	i (rad)	Ω (rad)	ω (rad)	M (rad)
3-days orbit	87865	0.917	0.5585	0	0	2.33
1-day orbit	42241	0.778	0.6981	0	0	1.02

Table 1: Orbit Definition

Spacecraft	m (kg)	R (m)	A (m^2)	C_R
Occulter	200	1	3.1416	1.3
Coronagraph	200	0.75	1.7671	1.3

Table 2: Spacecraft Physical Characteristics

For the purpose of this study, our simulations focus on five hours of formation flying in coarse mode, and two hours in fine mode, for the two types of HEOs defined in Table 1. We limit our simulations to an orbit arc section sufficiently away from perigee passage to conform to PROBA-3 expected operating conditions. Specifically, the spacecraft altitude ranges between approximately 37000 km and 63000 km for the 1-day HEO, and between 150000 km and 158000 km for the 3-days HEO.

4.2 Experimental Platform

We have developed a Simulink$^{©}$ model under the Matlab$^{©}$ environment to test and compare the aforementioned control laws. The dynamics of each spacecraft have been propagated with a variable order Adams-Bashforth-Moulton integrator. The SRP model features the eclipse coefficient described in 2.2 for the shadow casted by the occulter on the coronagraph spacecraft, with a cylindrical model for the Earth shadow, and a conical model for the occulter shadow.[7]

The metrology system have been assumed to be affected by independent, and uncorrelated, errors in distance and angle. Two navigation modes have been considered that provide different levels of accuracy: Coarse and Fine.[8] Since the metrology system provides position but not velocity, an observer module has been included. This module has been designed as a Kalman Filter at steady-state with plant matrix A_c as in the control definitions. The process noise has been set up to 100 times the mismodeling errors to conceal the deterministic errors, which remain as 1% of the noise. According to Fig. 2, the mismodeling errors due to considering a constant A_c decrease as the spacecraft altitude increases up to $\sim 10^5$ km. At higher altitudes, the magnitude of the mismodeling errors keeps constant and equal to the relative accelerations due to the SRP. Thus, we have selected a process noise level of 10^{-4} m/s^2 in standard deviation for altitudes ranging from 37000 km to 63000km, and a noise level of 10^{-5} m/s^2 for altitudes 150000 km to 158000 km. Regarding the measurement noise, the correlation between different coordinates of the observations have not been considered within the filter and the measurement covariance matrix has been setup as a diagonal matrix with diagonal elements equal to $10 \cdot \max\{\sigma_{range}, l * \sin(\sigma_{angle})\}^2 \cdot I_3$. The factor 10 has been included for conservativeness.

For a spacecraft separation of 150 m, the resultant observational errors due to the metrology system are 1 cm in the direction along the two spacecraft (see 4.1) both in coarse and fine navigation modes, but 2.6 m and 0.7 mm in the perpendicular direction in the coarse and fine modes, respectively. When the control system is enabled, the inter-vehicle distance should be

close to the baseline distance (150 m), and the performances of the metrology system should not vary significantly. Under these conditions, the Root Mean Square (RMS) of the navigation errors, are, approximately 27 cm in position and 3 cm/s in velocity in coarse mode, and 0.93 cm in position and 0.016 cm/s in velocity in fine mode.

According to the characteristics of present orbits, we have considered time windows of 2 hours for the time invariant linear approximations of the dynamic system. During these intervals, the variations on the plant matrix A_c are minimal with a negligible impact on the control gain matrices. Thus, these gain matrices are updated every 2 hours. The reference position for the coronagraph has been assumed to be known by the controller with no error. No Earth eclipses have been considered during current simulations, i.e., the occulter spacecraft has been assumed to be under full illumination during the complete orbit passage. Main physical limitations of the thrusters have been taken into account: the saturation of the thruster, and its resolution by considering a maximum thrust and quantize the control output.

5. RESULTS AND DISCUSSION

Using the scenario and platform just described, we performed simulations to test the performances of the three controls defined above. Since the performance depends critically on the values adopted for the specific parameters involved in the definition of each control law, we first discuss the optimal tuning of these parameters.

5.1 Control tuning

Fig. 7 illustrates the performances of the nonlinear control under different configurations, for the case of 1-day orbit and coarse navigation. The top panel corresponds to an optimal configuration, defined as one whereby the position error decreases to the expected noise level in a relatively short time span. For this particular control and simulation, we find that an optimized configuration can be achieved with parameter values $\alpha = 10^{-4}$ and $\beta = 10^{-2}$. In contrast to this, the middle and bottom panels of Fig. 7 show two examples of non-optimal configurations resulting from excessively small α and β values, respectively. As discussed in 3.1, small α values result in position variations that hardly depend on the relative positions, and the convergence to the reference position is excessively slow, whereas small β values results in fast motions towards the reference position and large relative velocities, which cause significant oscillations.

The configuration of the KNV control depends only on one parameter: the $bandwidth$. In this case, the ratio between the position and velocity weights within the controller are optimized within the KNV algorithm, thus, the strategy to tune the nonlinear control does not apply to this control. The $bandwidth$ parameter shall be tuned according to the convergence speed requirements while avoiding thrust saturation. The simulations show that $bandwidth = 0.01$ is close to the maximum value before thrust saturation, thus leading to a fast convergence.

The optimum solution of the LQR depends on the definition of the cost function J, which depends on the Q and R weighting matrices. In the present study, we will define these matrices according to the maximum size technique, i.e., defining a maximum error in position and velocity, p_{max}, v_{max}, a maximum control input u_{max}, and define the matrices as,

$$Q = \begin{pmatrix} p_{max}^{-2}I_3 & 0_3 \\ 0_3 & v_{max}^{-2}I_3 \end{pmatrix} \text{ and } R = u_{max}^{-2}I_3.$$

The definition of the values p_{max}, v_{max}, and u_{max} will obviously depend on the control mode (coarse or fine). The ratio between the maximum position and velocity values will, in fact, play

exactly the same role as the α and β values of the nonlinear control. Too large values for v_{max} results in position variations that hardly depend on the relative positions, and the convergence to the reference position is excessively slow. On the contrary, large p_{max} values yield to fast movements towards the reference position with large relative velocities that result in significant oscillations as in Fig. 7. The optimum values for the current scenarios have been found to be close to $(p_{max}, v_{max}, u_{max}) = (0.1, 10^{-3}, 10^{-5})$ in coarse mode, and $(10^{-3}, 10^{-5}, 10^{-7})$ in fine mode.

The optimum configurations for the three algorithms in fact, are closely related. The optimized α and β values are almost identical to the a and b values resulting from the optimized Q and R definitions; and the optimized $bandwidth$ corresponds to the norm of the poles of the closed system when considering the nonlinear control or the LQR control.
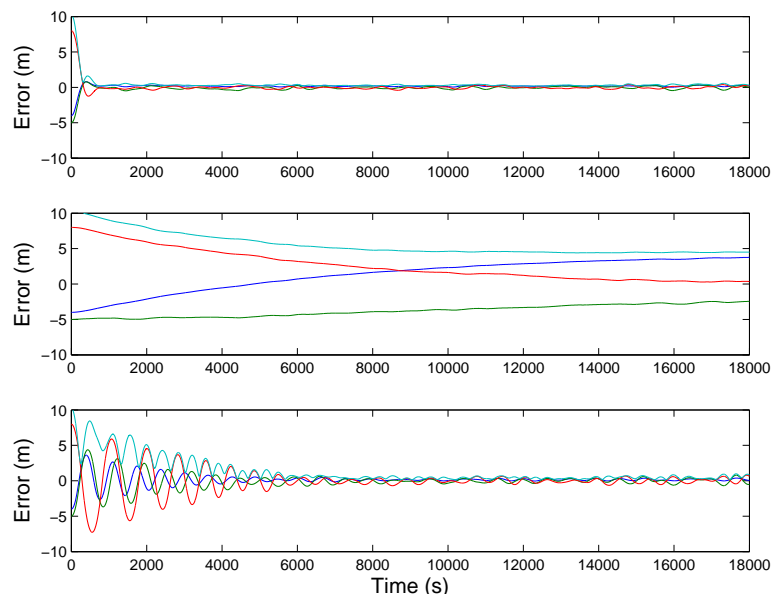
Fig. 7: Nonlinear control error under different configurations during coarse navigation along the 1-day orbit passage for (top) $\alpha = 10^{-4}$ and $\beta = 10^{-2}$, (middle) $\alpha = 10^{-6}$ and $\beta = 10^{-2}$, and (bottom) $\alpha = 10^{-4}$ and $\beta = 10^{-3}$. In all panels, colors show the error in (blue) x, (ref) y, and (green) z component of relative position.

5.2 Comparison of control performances

In this subsection, we will compare the performances of the controls under the optimized configurations. The initial control error before enabling the control system is assumed to be 10 m. In the coarse mode, all controls reach the steady-state in less than 15 min, and reduce the errors to less than half a meter in RMS, therefore, we will assume that the error is 0.5 m before switching to fine mode. In this mode, the system will reach again the steady-state in less than 15 min under any of the control algorithms. Table 4 summarizes the control performances at steady-state.

As it can be observed from this table, all controls provide reasonable and quite similar performances, in terms of e_c. Although the inclusion of an accurate model of the relative accelerations in the control definition can improve the performances in some scenarios, its omission

	1-day orbit passage		3-days orbit passage	
	Coarse	Fine	Coarse	Fine
Nonlinear	32	0.6	13	0.5
KNV	40	1.5	22	0.7
LQR	34	1.7	13	0.5

Table 3: RMS of control error in cm.

does not prevent the controls to get reasonably good performances thanks to the forcing of the cancellation of e_c through the linear term $K_H e_c$.

The algorithms that provide better performances are, in general, the nonlinear and the LQR controls. The higher errors of the KNV control are due to an unsuitable selection of the poles in section 3.2. From previous results, it seems that some of the poles of the system are not far enough from the positive side of the complex plane for the optimum $bandwidth$, and using larger $bandwidth$ values for the definition of the poles, which would increase the distance to this semi-plane, results in long lasting thrust saturation. A definition of the pole locations closer to the ones of the nonlinear, and the LQR controls (see Fig. 4) should provide better results.

In three out of the four scenarios that result from combining control mode and orbit passage, the performances of the nonlinear and LQR controls are quite similar. Fig. 8 shows an example of the control error performances corresponding to the 1-day orbit passage in coarse mode using the nonlinear control. The similar results between both controls in these three scenarios can be explained by the large magnitude of the linear term $K_H e_c$ of the nonlinear control in comparison with the relative acceleration term. As an example, the magnitude of the control input for the previous scenario is depicted in Fig. 9. Notice that the magnitude of the control input at steady-state is of the order of $5 \cdot 10^{-5} \ m/s^2$, which is one order of magnitude larger than the relative accelerations (see Fig. 2). As a result the only real difference between both controls is concealed (see Eq. (10)).
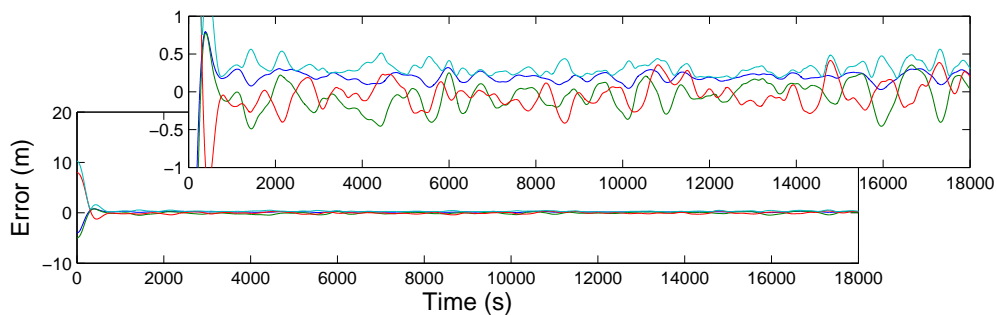
Fig. 8: Control error of the nonlinear control in coarse mode along the 1-day orbit passage. x, y, and z components of e_c in blue, green, and red, respectively, and $||e_c||$ in cyan.

In the special scenario corresponding to the fine mode control along the 1-day orbit passage, the magnitude of the linear term reduces with respect to the coarse navigation and lets the relative acceleration term play a significant role within the nonlinear control reducing the error by a factor of 2.8 with respect to the LQR control. Note that, since the relative acceleration decreases with the altitude of the spacecraft, this term vanishes again compared to the linear term as the altitude of both spacecraft increase, which explains that no significant difference can be encountered between both controls in fine mode along the 3-days orbit passage.
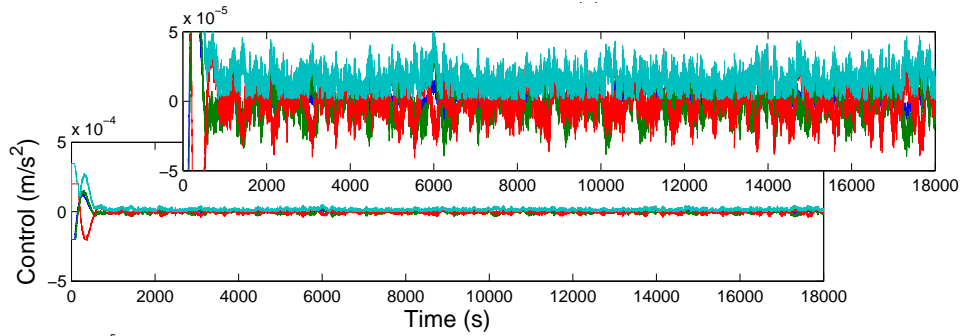
Fig. 9: Control input for the nonlinear control in coarse mode along the 1-day orbit passage.

Table 4 shows some statistics of the control input corresponding to the 1-day orbit passage in fine mode, where significant differences appear in the control error performances among different controls. First column contains the RMS of the control input at steady-state, and second contains the RMS of variations of the control input, i.e., $u(t_{i+1}) - u(t_i)$ for two consecutive control update instances, as an indicator of the control input oscillations. As it can be observed from these figures, the relative accelerations term within the nonlinear control yields to a significant reduction of the control oscillations compared to the remaining controls. The importance of this reduction resides on the subsequent reduction of the cumulative thrust necessary to keep the formation.

	u (m/s^2)	Δu (m/s^2)
Nonlinear	$8.4 \cdot 10^{-7}$	$9.5 \cdot 10^{-9}$
KNV	$1.1 \cdot 10^{-6}$	$2.3 \cdot 10^{-7}$
LQR	$9.6 \cdot 10^{-7}$	$2.9 \cdot 10^{-7}$

Table 4: Control input variations

The oscillations of the linear term $K_H e_c$ are mainly due to two factors, the navigation error included in the e_c computation; and the discretization of the control update, which currently occurs at the same rate of observation reception (1 Hz in coarse mode, and 10Hz in fine mode). A detailed analysis of the results have shown that, under current scenarios, the driver of the control oscillations is the error in the relative velocity. Therefore, an upgrade of the metrology system or the navigation filter to produce better relative velocity estimations may result in a significant improvement of the control performances.

6. SUMMARY AND CONCLUSIONS

In this document we have identified the Earth gravity and the Solar Radiation Pressure (SRP) as the major forces that drive the relative motion of two spacecraft in a virtual telescope formation, where one projects its shadow to the other. Since this shadow projects a narrow cone of umbra and penumbra, we have introduced a model which accounts for variations of the eclipse coefficient over the sun-facing surface of the coronagraph, or occulted spacecraft. We have designed several control laws and test its suitability for formation acquisition and formation keeping of a two spacecraft in formation for a virtual telescope.

In this study, we have tuned these controls for a PROBA-3 like scenario and compared the performances among them. The main conclusions of the results are as follows:

13 of 15

- The tuning of the control configuration parameters to obtain a gain feedback matrix can be a laborious task in general. The more suitable strategy to setup the control gain K_H is probably to define the Q and R matrices and compute a feedback matrix as the Linear Quadratic Regulator (LQR) solution. However, the physical insight of the α and β values also provide a reasonable method for tuning.

- Under the optimized configurations, all these controls can provide very similar performances and keep the formation within a maximum error of $\sim$ 50 cm in coarse mode, and 2 cm in fine mode along altitudes $\sim$ $30 - 40 \cdot 10^3$ km. At the maximum altitudes tested, $\sim$ $150 - 158 \cdot 10^3$ km, these errors reduce to 30 cm in coarse mode and 0.3 cm in fine mode.

- The inclusion of an accurate model for the relative accelerations, within the controller has an interesting benefit after formation acquisition, but never before. Thus, the computational burden associated to this term can be avoided till the formation is acquired. After that moment, the inclusion of the relative dynamics can significantly reduce the control error with no cost in terms of energy, or total Δv.

- The inclusion of the relative accelerations can reduce the control error by a factor of 2.8, as long as the magnitude of the linear term $K_H e_c$ is not larger than the relative acceleration, which occurs along low passages of the spacecraft under fine mode. In case the metrology system and the navigation filter provide better performances as the ones currently considered, the benefits of the relative acceleration term within the controller can be extended to higher altitudes.

ACKNOWLEDGMENTS

REFERENCES

[1] T. Rupp, S. D'Amico, O. Montenbruck, and E. Gill. Autonomous formation flying at DLR's German Space Operations Center (GSOC). In *Proceedings of the 58th International Astronautical Congress*, Hyderabad, India, September 2007.

[2] J. Kautsky, N. K. Nichols, and P. Van Dooren. Robust pole assignment in linear state feedback. *International Journal of Control*, 41(5):1129–1155, 1985.

[3] H. Kwakernaak and S. Raphael. *Linear Optimal Control Systems*. Wiley-Interscience, New York, 1972. Available at http://www.ieeecss.org/PAB/classics.

[4] B. Friedland. *Control System Design: An Introduction to State-Space Methods*. McGraw-Hill Higher Education, first edition, January 1985.

[5] E. D. Sontag. *Mathematical Control Theory. Deterministic Finite Dimensional Systems*. Texts in Applied Mathematics. Springer-Verlag, 1990.

[6] PROBA-3 phase A team. PROBA-3 phase A study executive summary report. Technical Report PROBA3-ASU-RPT-14, issue 01, EADS Astrium, December 2007.

[7] O. Montenbruck and E. Gill. *Satellite Orbits. Models, methods and applications*. Springer, Berlin, third edition, 2005.

[8] A. Wishart, F. Teston, S. Kemble, S. Grocott, A. Davies, C. Warren, and K. Geelen. The PROBA-3 formation flying technology demonstration mission. In *Proceedings of the 58th International Astronautical Congress*, Hyderabad, India, September 2007.

Perea, D'Amico, and Elosegui - (2009)

Appendix B

List of coauthors

D'Amico, Simone; Scientist at GPS Technology and Navigation Group at Deutsches Zentrum für Luft- und Raumfahrt (DLR); German Space Operations Center (GSOC), Münchner Strasse 20, 82234 Oberpfaffenhofen-Wessling, Germany; simone.damico@dlr.de.

Ardaens, Jean-Sébastien; Scientist at GPS Technology and Navigation Group at DLR; GSOC, Münchner Strasse 20, 82234 Oberpfaffenhofen-Wessling, Germany; jean-sebastien.ardaens@dlr.de.

Breger, Louis; Ph.D. Candidate at Massachusetts Institute of Technology (MIT) Department of Aeronautics and Astronautics; Building 33, Room 326, MIT, 77 Mass. Ave., Cambridge MA 02139, USA; lbreger@mit.edu.

Elosegui Larrañeta, Pedro; Senior scientist at Physics and Earth Observation Department at Instituto de Ciencias del Espacio (ICE); IEEC, Edifici Nexus, c/Gran Capità 2-4, 08034 Barcelona, Spain; pelosegui@ice.csic.es.

Gómez Muntané, Gerard; Full Professor at Applied Mathematics and Analysis Department at Universitat de Barcelona (UB); Gran Via 585, 08007 Barcelona, Spain; gerard@maia.ub.es.

How, Jonathan P.; Richard Cockburn Maclaurin Professor at Department of Aeronautics and Astronautics at MIT; Building 33, Room 326, MIT, 77 Mass. Ave., Cambridge MA 02139, USA; jhow@mit.edu.

Bibliography

[1] Announcement of Opportunity PROBA 3 Coronagraph. Technical Report D/SRE/DJS/PhE/og/25728, European Space Agency, Paris, France, July 2009.

[2] J. Borde, F. Teston, S. Santandrea, and S. Boulade. Feasibility of the PROBA 3 formation flying demonstration mission as a pair of microsats in GTO. In *Proceedings of the 55th International Astronautical Congress*, pages 1–12, Vancouver, Canada, Oct. 2004.

[3] R. A. Broucke. Motion near the unit circle in the three-body problem. *Celestial Mechanics and Dynamical Astronomy*, 73:281–290, 1999.

[4] J. A. Carrillo, M. Fornasier, J. Rosado, and G. Toscani. Asymptotic Flocking Dynamics for the kinetic Cucker-Smale model. Pre-print, Apr. 2009.

[5] J. A. Cañizo, J. A. Carrillo, and J. Rosado. A well-posedness theory in measures for some kinetic models of collective motion. July 2009. arXiv:0907.3901.

[6] F. Cucker and J. G. Dong. On the critical exponent for flocks under hierarchical leadership. *Mathematical Models and Methods in Applied Sciences*, 19:1391–1404, 2009.

[7] F. Cucker and C. Huepe. Flocking with informed agents. *MathS In Action*, 1(1):1–25, 2008. Class. Math.: 93C15.

[8] F. Cucker and S. Smale. Emergent behavior in flocks. *IEEE Transactions on Automatic Control*, 52:852–862, May 2007.

[9] S. D'Amico, J.-S. Ardaens, S. De Florio, and O. Montenbruck. Autonomous Formation Flying - TANDEM-X, PRISMA and Beyond. In *Proceedings of the 5th*

International Workshop on Satellite Constellations & Formation Flying, pages 1–15, Evpatoria, Crimea, July 2008.

[10] K. Danzmann. LISA mission overview. *Advances in Space Research*, 25:1129–1136, 2000.

[11] G. J. Ducard. *Fault-tolerant Flight Control and Guidance Systems. Practical Methods for Small Unmanned Aerial Vehicles.* Advances in Industrial Control. Springer London, 2009.

[12] C. P. Escoubet, M. Fehringer, and M. Goldstein. The Cluster mission. *Annales Geophysicae*, 19:1197–1200, 2001.

[13] D. Folta, F. Bauer, J. Leitner, J. P. How, M. Moreau, and R. Carpenter. Formation flight in space: Distributed spacecraft systems develop new GPS capabilities. *GPS World*, Feb. 2002.

[14] T. Fournier, J. Freymueller, and P. Cervelli. Tracking magma volume recovery at Okmok volcano using GPS and an unscented Kalman filter. *Journal of Geophysical Research*, 114:1–18, Feb. 2009.

[15] C. Fridlund. The Darwin mission. *Advances in Space Research*, 34:613–617, 2004.

[16] K. C. Gendreau, N. White, S. Owens, W. Cash, A. Shipley, and M. Joy. The MAXIM X-ray Interferometry Mission Concept Study. In *Proceedings of the 36th Liege International Astrophysics Colloquium*, pages 1–5, Liege, Belgium, July 2001.

[17] G. Gómez, M. Marcote, J. J. Masdemont, and J. M. Mondelo. Zero relative radial acceleration cones and controlled motions suitable for formation flying. *The Journal of the Astronautical Sciences*, 53:413–431, 2005.

[18] T. Grelier, A. Garcia, E. Péragin, L. Lestarquit, J. Harr, D. Seguela, J.-L. Illser, J.-B. Thevenet, N. Perriault, C. Mehlen, C. Ensenat, N. Whilhelm, A. M. Badiola Martinez, and P. Colmenarejo. Formation Flying Radio Frequency Missions, Techniques, and Technology. *InsideGNSS*, pages 40–46, Nov. 2008.

[19] G. M. Hoffmann. *Autonomy for sensor-rich vehicles: Interaction between sensing and control actions.* PhD thesis, Department of Aeronautics and Astronautics, Stanford University, Stanford, California, Sept. 2008.

[20] G. M. Hoffmann, S. L. Wasl, and C. J. Tomlin. Mutual information methods with particle filters for mobile sensor network control. In *IEEE Conference on Decision and Control*, pages 1019–1024, 2006.

[21] P. J. Huxel and R. H. Bishop. Fusing inertial and relative range measurements for inertial navigation in the presence of large state error covariances. In *Proceedings of the 16th AAS/AIAA Space Flight Mechanics Conference*, pages 1–17, Tampa, Florida, 2006.

[22] G. Inalhan, M. Tillerson, and J. P. How. Relative dynamics and control of spacecraft formations in eccentric orbits. *Journal of Guidance Control and Dynamics*, 25:48–59, Jan. 2002.

[23] A. Jadbabaie, J. Lin, and A. Morse. Coordination of groups of mobile autonomous agents using nearest neighbor rules. *IEEE Transactions on Automatic Control*, 48(6):988–1001, 2002.

[24] R. E. Kalman. A new approach to linear filtering and prediction problems. *Journal of Basic Engineering*, 82:35–45, 1960.

[25] L. Kaltenegger and C. Fridlund. The Darwin mission: Search for extra-solar planets. *Advances in Space Research*, 36:1114–1122, 2005.

[26] W. J. Larson and J. R. Wertz, editors. *Space Mission Analysis and Design*. Space Technology Library. 1999.

[27] J. Leitner. Formation flying technology. In *Space Technology 9 (ST9) workshop*, May 2003.

[28] M. Mandic. Distributed estimation architectures and algorithms for formation flying spacecraft. Master's thesis, Department of Aeronautics and Astronautics, Massachusetts Institute of Technology, June 2006.

[29] P. S. Maybeck. *Stochastic Models, Estimation and Control*. Academic Press, New York, NY, 1982.

[30] C. R. McInnes. Autonomous ring formation for a planar constellation of satellites. *Journal of Guidance, Control, and Dynamics*, 18(5):1215–1217, 1995.

[31] A. Miele, T. Wang, and W. Y. Lee. Optimization and guidance of trajectories for coplanar, aeroassisted orbital transfer. *Journal of the Astronautical Sciences*, 38:311–333, Sept. 1990.

[32] L. Perea, J.-S. Ardaens, S. D'Amico, and P. Elosegui. Relative Control of a Virtual Telescope in a High Elliptical Orbit using GNSS and Optical Metrology. *Journal of Guidance, Control, and Dynamics*, 2010. (Submitted).

[33] L. Perea, S. D'Amico, and P. Elosegui. Relative Formation Flying Dynamics and Control of a Two-Element Virtual Telescope on a HEO. In CNES, editor, *Proceedings of the 21st International Symposium on Space Flight Dynamics (ISSFD)*, pages 1–15, Sept. 2009.

[34] L. Perea and P. Elosegui. New State Update Equation for the Unscented Kalman Filter. *Journal of Guidance, Control and Dynamics*, 31(5):1500–1504, Sept. 2008.

[35] L. Perea, G. Gómez, and P. Elosegui. Extension of the Cucker–Smale Control Law to Space Flight Formations. *Journal of Guidance, Control, and Dynamics*, 32(2):527–537, 2009.

[36] L. Perea, J. How, L. Breger, and P. Elosegui. Nonlinearities in sensor fusion. Divergence issues in EKF, modified truncated SOF, and UKF. In AIAA, editor, *Proceedings of the AIAA Guidance Navigation and Control Conference and Exhibit*, pages 1–16, Aug. 2007. Paper No. AIAA-2007-6514.

[37] S. Persson, P. Bodin, E. Gill, J. Harr, and J. Joergenson. PRISMA - An Autonomous Formation Flying Mission. In *Proceedings of the Small Satellite Systems and Services - The 4S Symposium*, pages 1–12, Chia Laguna Sardinia, Italy, Sept. 2006.

[38] H. Plinval. Analysis of relative navigation architectures for formation flying spacecraft. Master's thesis, Department of Aeronautics and Astronautics, Massachusetts Institute of Technology, Feb. 2006.

[39] PROBA-3 phase A team. PROBA-3 phase A study executive summary report. Technical Report PROBA3-ASU-RPT-14, issue 01, EADS Astrium, Dec. 2007.

[40] PROBA-3 Team. Summary of PROBA 3 Mission Analysis for Coronagraph Instrument. Technical Report P3-EST-TN-7002, ESTEC, July 2009.

[41] M. Sabatini and G. B. Palmerini. Collective control of spacecraft swarms for space exploration. *Celestial Mechanics and Dynamical Astronomy*, 105:229–244, Mar. 2009.

[42] D. P. Scharf, F. Hadaegh, and S. R. Ploen. A survey of spacecraft formation flying guidance and control (part ii): Control. In *Proceedings of the American Control Conference*, pages 2976–2985, Boston, MA, June 2004.

[43] H. Schaub, S. R. Vadali, J. L. Junkins, and K. T. Alfriend. Spacecraft formation flying control using mean orbit elements. *The Journal of the Astronautical Sciences*, 48:69–87, 2000.

[44] H. Schlingloff. *Astronautical engineering: an introduction to the technology of spaceflight*. Hanfried Schlingloff, 2005.

[45] B. Tapley, S. Bettadpur, M. Watkins, and C. Reigber. The Gravity Recovery and Climate Experiment: Mission Overview and Early Results. *Geophysical Research Letters*, 31:1–6, 2004.

[46] W. Truszkowski, H. L. Hallock, C. Rouff, J. Karlin, J. Rash, M. Hinchey, and R. Sterritt. *Autonomous and Autonomic Systems: With Applications to NASA Intelligent Spacecraft Operations and Exploration Systems*. NASA Monographs in Systems and Software Engineering. Springer London, 2009.

[47] S. G. Ungar, J. S. Pearlman, J. A. Mendenhall, and D. Reuter. Overview of the Earth Observing One (EO-1) mission. *IEEE Transactions on Geoscience and Remote Sensing*, 41:1149–1159, June 2003.

[48] T. Vicsek, A. Czirok, E. Ben-Jacob, I. Cohen, and O. Sochet. Novel type of phase transition in a system of self-driven particles. *Physical Review Letters*, 75:1226, 1995.

[49] A. Wishart, F. Teston, S. Kemble, S. Grocott, A. Davies, C. Warren, and K. Geelen. The PROBA-3 formation flying technology demonstration mission. In *Proceedings of the 58th International Astronautical Congress*, pages 1–10, Hyderabad, India, Sept. 2007.

[50] K. Yamanaka and F. Ankersen. New state transition matrix for relative motion on an arbitrary elliptical orbit. *Journal of Guidance, Control, and Dynamics*, 25(1):60–66, 2002.

[51] *DARWIN mission home page.* European Space Agency, Nov. 2009. `http://www.esa.int/science/darwin`.

[52] *DARWIN Exoplanet Space Mission home page.* Council for the Central Laboratory of the Research Councils, Nov. 2009. `http://www.darwin.rl.ac.uk/`.

[53] *SIMBOL-X mission home page.* Centre National d'Etudes Spatiales, May 2008. `http://smsc.cnes.fr/simbolx`.

[54] *SIMBOL-X mission.* Agenzia Spaziale Italiana, Nov. 2009. `http://www.asdc.asi.it/simbol-x`.

Nomenclature

Roman Symbols

A	Dynamics matrix; deterministic matrix; or the area of Sun exposition of a spacecraft
a	State transition matrix; semi-major axis; the acceleration vector; or the weighting function of the CS model
A_x	Adjacency matrix
AU	Astronomical unit (149598000 km)
B	Deterministic matrix; or polynomial coefficient
b_m	Second order term of the mtSOF
C	Observations matrix
C_R	Radiation pressure coefficient of the satellite surface
d	Time derivative; or distance
D_x	Derivative with respect to x
D_x	Diagonal matrix
E	Expectation value
e	Error vector; eccentricity; or 2.7183
f	Dynamic model function

G	Driver function for the Brownian motion
g	Generic function
GM	Gravitational parameter
H	Jacobian of h, i.e. $D_x h$; or Hurwitz matrix
h	Measurement model function
I	Improvement indicator of filters
i	Index; orbital inclination; and the integral of the position; or $\sqrt{-1}$
J	Jacobian of the inverse of h, i.e. $D_x(h^{-1})$; or cost function
K	Gain matrix; a multiplier coefficient of the CS model; or the reflectivity ratio $C_R A/m$
l	Reference separation between the occulter and the coronagraph spacecraft
$L1$	GPS frequency for civilian use
$L2$	Second libration point of the Sun-(Earth+Moon) system
L_x	Laplacian of the adjacency matrix A_x
M	Mean anomaly
m	Dimension; or the mass of a spacecraft
N	Number of corrective maneuvers associated to one control maneuver
n	Dimension of the state space; or order of the harmonic decomposition
$N_m(a, B)$	Normal distribution of dimension m with a mean and B variance

$NavSet$ Flags the availability of relative acceleration data within the navigation data set

P Solution of the CARE

p Dimension; or position vector

$P = P_{xx}$ State covariance matrix

$P_\odot$ Force per unit area exerted by the SRP ($4.56 \cdot 10^{-6} \ N/m^2$)

P_{xz} State-measurements correlation matrix

P_{zz} Measurements covariance matrix

Q Process noise matrix; Inner product associated to the CS model; or positive definite weight matrix

q Dimension

R Measurement noise matrix; radius of the sun facing surface of a spacecraft; or positive definite weight matrix

r Range; or position vector

S Sun facing surface of a satellite

s Time

t Time

T_m Time step between correction maneuvers

T_t Time step between control maneuvers

u Control input; or unitary vector

v A noise realization; or the velocity vector

W Specific set of weights for the UKF

w Noise realization

x State vector. Depending on the context, it may include the velocity

y, z Observation vector

Greek Symbols

α Angle; or a positive scalar

β Brownian motion; a positive scalar; or the exponential coefficient of the CS model

Δ Differential value

η Coefficient to account for the shadow projected by the occulter spacecraft to a surface point

Γ Deterministic matrix; or half of the square of relative positions

Λ Half of the square of relative velocities

μ Mass parameter

ν Earth-shadow coefficient

Ω Right ascension of the ascending node

ω Argument of perigee

∂ Partial derivative

π Partition of a time interval; or Pi (≈ 3.1416)

σ Standard deviation; or the offset coefficient of the CS model

θ Angle

φ Coefficient to account for the shadow projected by the occulter spacecraft to the coronagraph spacecraft

Superscripts

$UKFz$ Unscented Kalman Filter with residuals modification

UKF	Unscented Kalman Filter	$distance$	Distance
$\cdot$	Time derivative	$drag$	Atmospheric drag contribution
$\wedge$	Estimated value	k	Iterate number; or number of elements in the spacecraft formation
$\wedge$	Limit when $t \to \infty$		
$+$	A posteriori estimation		
$-$	A priori estimation	new	Newer definition
T	Matrix/vector transpose	os	Occulter spacecraft
(c)	Relative to the covariance	$others$	Lower order contributions
(m)	Relative to the mean	$range$	Range observations
-1	Inverse operator	$ref, true$	Reference value
j	Index	r	Range
		$sh, n > 0$	Contribution due to the spherical harmonics of positive order ($n > 0$) of the geopotential

Subscripts

$\odot$	Sun		
$\oplus$	Earth	SRP	Contribution due to the Solar Radiation Pressure
θ	Angle		
H	Hurwitz matrix	**Other Symbols**	
i, j	Index	$'$	Time derivative
K	KNV control	0_n	Zero matrix of dimension n
L	LQR control	$\mathbb{N}$	Natural numbers set
M	Moon	$\mathbb{R}^n$	State space
max	Maximum value	$\mathcal{F}$	Filtration
min	Minimum value	$\mathcal{L}.\cdot$	Lie derivative
0	Initial condition	$\mathcal{O}$	Order of the error
$angle$	Angle observations	$\mathcal{X}$	Sigma set of points of the UKF
B	Barycenter of the constellation	$\mathcal{Z}$	Observations associated to the sigma set $\mathcal{X}$
CM	Contribution due to the gravity constant		
cs	Coronagraph spacecraft	$\otimes$	Kronecker product
c	Control	I_n	Identity matrix of dimension n

List of acronyms

AAS   American Astronomical Society

AIAA   American Institute of Aeronautics and Astronautics

B-EKF   Bump-up Extended Kalman Filter

B-mtSOF   Bump-up modified truncated Second Order Filter

B-UKF   Bump-up Unscented Kalman Filter

CARE   Continuous Algebraic Ricatti Equation

CLS   Coarse Lateral Sensor

CS   Cucker-Smale

CSA   Canadian Space Agency

CSIC   Consejo Superior de Investigaciones Científicas

DLR   Deutsches Zentrum für Luft- und Raumfahrt

DWI   Dual Wavelength Interferometer

ECEF   Earth-Centered Earth Fixed

ECI   Earth-Centered Inertial

EKF   Extended Kalman Filter

EO-1   Earth Observing One

ESA   European Space Agency

LIST OF ACRONYMS

ESTEC   European Space Research and Technology Centre

FCC   Flight Control Computer

FF   Formation Flying

FFTB   Formation Flying Testbed

FFRF   Formation Flying Radio Frequency

FLS   Fine Lateral Sensor

GIF   GPS interface

GNC   Guidance, Navigation, and Control

GNSS   Global Navigation Satellite System

GOD   GPS Orbit Determination

GOP   GPS Orbit Prediction

GPS   Global Positioning System

GRACE   Gravity Recovery and Climate Experiment

GRAPHIC   Group and Phase Ionospheric Correction

GSF   Gauss Second-Order Filter

GSOC   German Space Operations Center

GSS   GNSS Signal Simulator

GSTP   General Support Technology Programme

H-C   Hill-Clohessy-Wiltshire

HEO   High Elliptical Orbit

HW   Hardware

ICE   Instituto de Ciencias del Espacio

IEEC	Institut d'Estudis Espacials de Catalunya
IEEE	Institute of Electrical and Electronics Engineers
IEKF	Iterative Extended Kalman Filter
INS	Inertial Navigation System
IRF	Inertial Reference Frame
IUKF	Improved Unscented Kalman Filter
JAXA	Japan Aerospace Exploration Agency
JGCD	Journal of Guidance, Control, and Dynamics
KF	Kalman Filter
KNV	Kautsky-Nichols-Van Dooren
LEO	Low Earth Orbit
LISA	Laser Interferometer Space Antenna
LOS	Line of Sight
LQR	Linear Quadratic Regulator
LQRI	Linear Quadratic Regulator with the Integral term
LRKF	Linear Regression Kalman Filters
LSQ	Least Squares Filter
MAXIM	Micro Arcsecond X-Ray Imaging Mission
MEO	Medium Earth Orbit
MICINN	Ministerio de Ciencia y Innovación
MIT	Massachusetts Institute of Technology
MMS	Magnetospheric Multi-Scale

LIST OF ACRONYMS

MPC	Model Predictive Control
MSR	Mars Sample Return
mtSOF	Modified truncated Second Order Filter
NASA	National Aeronautics and Space Administration
NDI	Non-Linear Dynamic Inversion
OBC	Onboard Computer
PC	Personal Computer
PID	Proportional-Integral-Derivative
PF	Particle Filters
PI	Planet Imager
POE	Planetary Orbital Environment
PPS	Pulse Per Second
PROBA	Project for Onboard Autonomy
RdV	Rendezvous
RF	Radio Frequency
RMS	Root Mean Square
RTBP	Restricted Three Body Problem
SAR	Synthetic Aperture Radars
SOF	Second Order Filters
SRP	Solar Radiation Pressure
SW	Software
TPF	Terrestrial Planet Finder

UB   Universitat de Barcelona

UKF   Unscented Kalman Filter

UKFz   Unscented Kalman Filter with residuals modification

XEUS   X-ray Evolving Universe Spectroscopy

Y-A   Yamanaka-Ankersen

ZRRAC   Zero Relative Radial Acceleration Cones